

The A' Experiment (APEX): Search for a New Vector Boson A' Decaying to e^+e^-

A Proposal to Jefferson Lab PAC37

J.D. Bjorken, **R. Essig (co-spokesperson)**

Theory Group, SLAC National Accelerator Laboratory, Menlo Park, CA 94025

P. Schuster (co-spokesperson), N. Toro (co-spokesperson)

Perimeter Institute for Theoretical Physics, Waterloo ON, Canada

K. Allada, P. Bosted, J. Boyce, P. Brindza, A. Camsonne, E. Chudakov,
M. Dalton, A. Deur, A. Gavalya, J. Gomez, C.W. de Jager, E. Folts, J.-O. Hansen,

D. W. Higinbotham, J.J. LeRose, D. Meekins, R. Michaels, S. Nanda,

Y. Qiang, Y. Roblin, A. Saha, B. Sawatzky, J. Segal, S. Stepanyan,

B. Wojtsekhowski (co-spokesperson and contact), J. Zhang

Thomas Jefferson National Accelerator Facility, Newport News, VA 23606

C. Field, M. Graham, J. Jaros, T. Maruyama, J. McDonald,

K. Moffeit, A. Odian, M. Oriunno, R. Partridge, D. Waltz

SLAC National Accelerator Laboratory, Menlo Park, CA 94025

J. Beacham, K. Cranmer

New York University, NY

S. Abrahamyan, S. Malyan, A. Shahinyan

Yerevan Physics Institute, Armenia

E. Aliotta, A. Barbieri, R. Lindgren, N. Liyanage, V. Nelyubin,

B.E. Norum, K. Saenboonruang, M.H. Shabestari, W.A. Tobias

University of Virginia, Charlottesville, VA 22901

K. Aniol, S. Iqbal, D. J. Magaziotis

California State University, Los Angeles, CA 90032

J. Bono, P. Markowitz, V. Maxwell

Florida International University, Miami, FL 33199

A. Glamazdin

Kharkov Institute of Physics and Technology, Kharkov 310077, Ukraine

S. Gilad, J. Huang, A. Kelleher, S. Riordan, V. Sulkovsky

Massachusetts Institute of Technology, Cambridge, MA 02139

M. Khandaker, V. Punjabi

Norfolk State University, Norfolk, VA 23504

L. El Fassi, R. Gilman, G. Kumbartzki, R. Ransome, Y. Zhang
Rutgers, The State University of New Jersey, Piscataway, NJ 08854

S. Beck, O. Hen, I. Korover, E. Piasetzky, I. Pomerantz, R. Shneur

Tel Aviv University, Israel

D. Armstrong, T. Averett, W. Deconinck, E. Jensen, B. Zhao
College of William and Mary, Williamsburg, VA 23185

M. Mihovilovič, S. Širca
Jožef Stefan Institute and Dept. of Physics, University of Ljubljana, Slovenia

G. Ron
Hebrew University of Jerusalem, Jerusalem, Israel

A. Afanasev
Hampton University, VA

Z. Ahmed
Syracuse University, NY

D. Anez
Saint Mary's University, Halifax, NS

K. Bartlett, J. Donaghy, M. Holtrop
University of New Hampshire, NH

N. Bubis
Technion, Israel

A. Gasparian
North Carolina Agricultural and Technical University, NC

N. Goeckner-Wald
Carnegie-Mellon, PA

T. Holmstrom
Longwood University, Farmville, VA 23909

E. Long, L. Selvy
Kent State University, OH

J. Mammei
University of Massachusetts, MA

M. Paolone
South Carolina University, SC

X. Jiang, A. Puckett
Los Alamos National Laboratory, Los Alamos, NM 87545

R. Subedi
George Washington University, DC

C.E. Hyde, L. Weinstein
Old Dominion University, Norfolk VA

The Hall A Collaboration

December 1, 2010

Abstract

The A' EXperiment (APEX) is proposed to search for a new vector boson A' with weak coupling $\alpha' \gtrsim 9 \times 10^{-8} \alpha$ to electrons ($\alpha = e^2/4\pi$) in the mass range $65 \text{ MeV} \lesssim m_{A'} \lesssim 525 \text{ MeV}$. New vector bosons with such small couplings arise naturally from a small kinetic mixing of the “dark photon” A' with the photon — one of the very few ways in which new forces can couple to the Standard Model — and have received considerable attention as an explanation of various dark matter related anomalies. A' bosons are produced by radiation off an electron beam, and could appear as narrow resonances with small production cross-section in the trident e^+e^- spectrum. We propose to search for the A' by using the CEBAF electron beam at energies of $\approx 1\text{-}4 \text{ GeV}$ incident on $0.7 - 8\%$ radiation length Tungsten multi-foil targets, and measure the resulting e^+e^- pairs using the High Resolution Spectrometer and PREX septum magnet in Hall A at Jefferson Lab. With a 34-day run, the proposed experiment will achieve very good sensitivity because the statistics of e^+e^- pairs will be 10,000 times larger than any previous search for the A' boson. These statistics and the excellent mass resolution of the spectrometers allow sensitivity to α'/α two to three orders of magnitude below current limits, in a region of parameter space of great theoretical and phenomenological interest.

Contents

1	Introduction	1
1.1	Brief overview of the proposed experiment	1
1.2	The impact of this experiment	2
1.3	Changes from the proposal submitted to PAC 35	2
1.4	The organization of this proposal	3
2	Physics	3
2.1	Motivation for New Physics Near the GeV Scale	3
2.2	Motivation for an A' from Dark Matter	7
2.3	Existing constraints	10
2.4	Potential Improvements From Existing Data	11
3	The production of an A' in fixed target collisions	12
4	Experimental setup	14
4.1	Concept of the experiment	14
4.2	The multi-foil target	15
4.3	The room temperature septum magnet	21
4.4	The detector package	21
4.5	Identification of electrons and positrons	22
4.6	Measurement of the particle track	23
4.6.1	High-rate operation of the VDC	23
4.7	Trigger and DAQ configurations	25
4.8	HRS optics quality	25
4.9	Parameters of the HRS	26
5	Signal and Trident Kinematics and Search Strategy	26
5.1	Statistical Analysis for Peak Search and Limit-Setting	29
5.1.1	Searching for a Resonance: a rough preliminary outline	29
5.1.2	Setting Limits on α'/α	31
5.2	Smoothness of the invariant mass acceptance	32
5.3	Calculation of the ϵ reach	33
6	Backgrounds	35
6.1	Inclusive rates	35
6.1.1	The electron singles rates in HRS	37
6.1.2	The pion singles rates in the HRS	37
6.1.3	The proton singles rates in HRS	39
6.2	True and accidental coincidences	39
6.3	Electron-Positron Pairs from Conversion of Real Photons	40
7	Proposed measurements	41
7.1	Beam time request	42

8	The concerns identified by PAC35	44
8.1	The PAC35 report	45
8.2	The multi-foil target (reviewer's comment 1)	46
8.3	The relative angular resolution (reviewer's comment 2)	46
8.4	Particle identification (reviewer's comment 3)	47
8.5	The lead glass calorimeter PID at high event rate (reviewer's comment 3) . .	48
8.6	The gas Cherenkov PID at high event rate (reviewer's comment 3)	48
8.7	Backgrounds (reviewer's comments 4)	50
8.7.1	Test Run results	51
8.7.2	Background rate	51
8.8	Acquisition and trigger rate (reviewer's comment 5)	51
8.9	The short coincidence time window (reviewer's comment 5)	52
8.10	The high rate operation of the VDC (reviewer's comment 6)	52
8.11	Septum magnet (reviewer's comment 7)	54
8.12	Summary	54
9	Conclusion	55
A	Effective Photon Flux, Target Nucleus and Beam-Energy Dependence	56
B	Mass resolution	57

1 Introduction

The development of the Standard Model of particle interactions is the culmination of a century of searches and analysis with fixed-target and colliding beam experiments. Interactions with new forces beyond the Standard Model are currently limited by well-tested gauge symmetries to a handful of possibilities. The only remaining way for interactions with new sub-GeV vector-like forces to arise is for charged particles to acquire millicharges, ϵe , under these forces (here e is the coupling between the photon and the charged particle). This occurs through a simple and generic mechanism proposed by Holdom [1], in which a new vector particle A'_μ mixes via quantum loops with the Standard Model photon. MeV–GeV masses for the A' gauge boson are particularly well-motivated in this context. Such sub-GeV forces are a common feature of extensions of the Standard Model, but existing constraints are remarkably weak, with limits at $\epsilon e \lesssim (0.3 - 1) \times 10^{-2}e$.

Modern high-intensity 100% duty factor beams and existing precision spectrometers are ideally suited to explore sub-GeV forces by probing reactions in which a new A' vector particle is produced by radiation off an electron beam. The A' decays to an electron and positron pair and appears as a narrow resonance of small magnitude in the invariant mass spectrum. The production rate of A' s, the luminosity, and the mass resolution attainable at Jefferson Laboratory vastly exceeds what is currently available using colliding electron beam facilities. For these reasons, we propose a dedicated search using Jefferson Laboratory’s Continuous Electron Beam Accelerator Facility (CEBAF) and the High Resolution Spectrometers (HRS) in Hall A. The proposed experiment will probe charged particle couplings with new forces as small as $2 \times 10^{-4}e$ and masses between 65 MeV and 525 MeV — an improvement by more than two orders of magnitude in cross section sensitivity over all previous experiments.

This experiment is particularly timely in light of a series of recent anomalies from terrestrial, balloon-borne, and satellite experiments that suggest that dark matter interacts with Standard Model particles. Much of this data hints that dark matter is directly charged under a new force mediated by an A' and not described by the Standard Model. Theoretical as well as phenomenological expectations suggest an A' mass $m_{A'} \lesssim 1 \text{ GeV}$ and $\epsilon e \lesssim 10^{-2}e$. Much of this region will be explored with the proposed experiment.

1.1 Brief overview of the proposed experiment

The experiment will measure the invariant mass spectrum of electron-positron pairs produced by electron scattering on a high- Z Tungsten multi-foil target. The spectrum will be scanned in the wide mass range of 65 MeV to 525 MeV for a narrow peak with a width corresponding to the instrumental resolution. Using single-arm distributions, the acceptance of the experiment will be precisely determined. The electron and positron will be detected in the magnetic spectrometers. For the mass range of interest, the spectrometer will be configured, using the recently constructed septum magnet, to detect electrons and positrons scattering at small angles [2]. The relative mass resolution will be roughly 0.5%, limited primarily by multiple scattering in the target material.

The central angle for spectrometers with nominal target position will be 5° as for the ^{208}Pb Radius Experiment (PREX). The e^+e^- pairs will be detected in coincidence within a timing window of 20 ns. The rejection of pion backgrounds will be done online by using the shower calorimeters and the gas Cherenkov counters. With a beam of $\lesssim 80 \mu\text{A}$ on 0.5%–10% radiation-length targets at various beam energies, we expect to collect true coincidence e^+e^-

events with a rate in the range 100–500 Hz. The total e^+e^- sample size will exceed 10^8 pairs in a 6-day period for each setting. Each kinematic setting will cover an $\mathcal{O}(1)$ interval of the e^+e^- invariant mass range.

We propose a run plan for the 12 GeV running period, using a setting with beam energy 2.2 GeV for 6 days and setting with beam energy 4.4 GeV for 12 days. We additionally propose to use 6 days at 1.1 GeV and 3.3 GeV. We emphasize that this experiment is ready to run on short notice. The only special equipment required is a new multi-foil target, which has already been constructed and is ready to be used.

1.2 The impact of this experiment

The proposed experiment will be sensitive to new gauge bosons with couplings $\epsilon e \gtrsim 3 \times 10^{-4} e$, corresponding to cross-section suppression $\alpha'/\alpha \gtrsim 9 \times 10^{-8}$ – see Figure 1. This is about a factor of 10–30 times lower in ϵ than existing constraints (which assume that the A' couples also to muons), and corresponds to 100–1000 times smaller cross-sections.

This parameter range is interesting for several reasons. This region of mass and coupling is compatible with A' 's explaining the annual modulation signal seen by the dark matter direct detection experiment DAMA/LIBRA, and also with dark matter annihilating or decaying into A' 's, which explains a myriad of recent cosmic-ray and other astrophysical anomalies (see Section 2.2). The region is also compatible with A' 's explaining the discrepancy between the Standard Model predicted and measured value of the anomalous magnetic moment of the muon, $(g-2)_\mu$. In addition, and independently of any connection to dark matter, the proposed experiment would be the first to probe A' 's of mass ~ 100 MeV with gauge kinetic mixing below $\epsilon \sim 10^{-3}$, the range most compatible if the Standard Model hypercharge gauge group is part of a Grand Unified Theory.

The importance for fundamental physics of discovering new forces near the GeV scale cannot be overstated.

1.3 Changes from the proposal submitted to PAC 35

A previous version of this proposal has been submitted to PAC 35. It has been conditionally approved by PAC 35, which stated that “The high impact on the global physics scene of [these] measurements makes this experiment [a] high priority”. We had a test run in June/July 2010 with several days of beam for testing the performance of the detectors and the HRS's at conditions close to the 2.2 GeV proposed setting of this proposal. With the data collected during the test run, we are able to address the majority of the PAC 35 concerns.

We are re-submitting the complete proposal to PAC 37 with several sections updated. The updates include:

- The theory motivation (Section 2) was updated to reflect some of the exciting new developments in the past year.
- A special multi-foil target was constructed for the test run, although it was never installed due to time constraints. The multi-foil target presents a superior design over that originally described in the PAC 35 proposal. We describe the new target in detail in Section 4.

- We have updated the discussion of the particle identification in Section 4.5, to be consistent with what has been found in the test run data (Section 8.4).
- We discuss in more detail our strategy to search for a resonance and, if no resonance is found, how we plan to set limits (Section 5).
- In Section 8, we provide a detailed response to the PAC 35 concerns.

1.4 The organization of this proposal

The proposal is organized as follows. In Section 2, we present the physics of hypothetical A' particles, motivation for its existence, and limits from existing data. In Section 3, we describe A' production in fixed-target experiments. In Section 4, we describe the experimental approach, including the standard equipment and the multi-foil target we intend to use for this experiment. In Section 5, we present the parametrics and the Monte Carlo (MC) simulations of the QED e^+e^- pair production rate and the A' signal rate in the proposed setup. We also describe how we made the sensitivity plots. The search procedure for the A' and our strategy for setting limits is also presented. Other background rates, such as π^+ or e^+ singles and accidental e^+e^- pairs, are discussed in Section 6. The expected results and requested beam time are discussed in Section 7. The issues indentified by PAC35 and some of the test run results are discussed in Section 8. The advances in HRS optics calibration and data analysis are presented. The proposal is summarized in Section 9. Two appendices discuss the form factors used to calculate the signal and background rates (Section A) and the mass resolution (Section B).

2 Physics

We propose to search for new sub-GeV mass vector bosons — ‘dark photons’, A' — that couple very weakly to electrons. It is useful to parameterize the coupling g' of the A' to electrons by a dimensionless $\epsilon \equiv g'/e$, where e is the electron charge. Cross-sections for A' production then scale as $\alpha'/\alpha = \epsilon^2$, where $\alpha' = g'^2/(4\pi)$ and $\alpha = e^2/(4\pi)$ are the fine-structure constants for the dark photon and ordinary electromagnetic interactions. This experiment will search for A' bosons with mass $m_{A'} \sim 65 \text{ MeV} - 525 \text{ MeV}$ and $\alpha'/\alpha \gtrsim 9 \times 10^{-8}$, which can be produced by a reaction analogous to photon bremsstrahlung (see Section 3) and decays promptly to e^+e^- or other charged particle pairs. We refer the reader to Figure 1 for a summary of the reach of this experiment.

2.1 Motivation for New Physics Near the GeV Scale

New light vector particles, matter states, and their associated interactions are ubiquitous in extensions of the Standard Model [1, 9, 10, 11, 12, 13]. However, the symmetries of the Standard Model restrict the interaction of ordinary matter with such new states. Indeed, most interactions consistent with Standard Model gauge symmetries and Lorentz invariance have couplings suppressed by a high mass scale. One of the few unsuppressed interactions is the coupling of charged standard model particles ψ

$$\delta\mathcal{L} = g' A'_\mu \bar{\psi} \gamma^\mu \psi \quad (1)$$

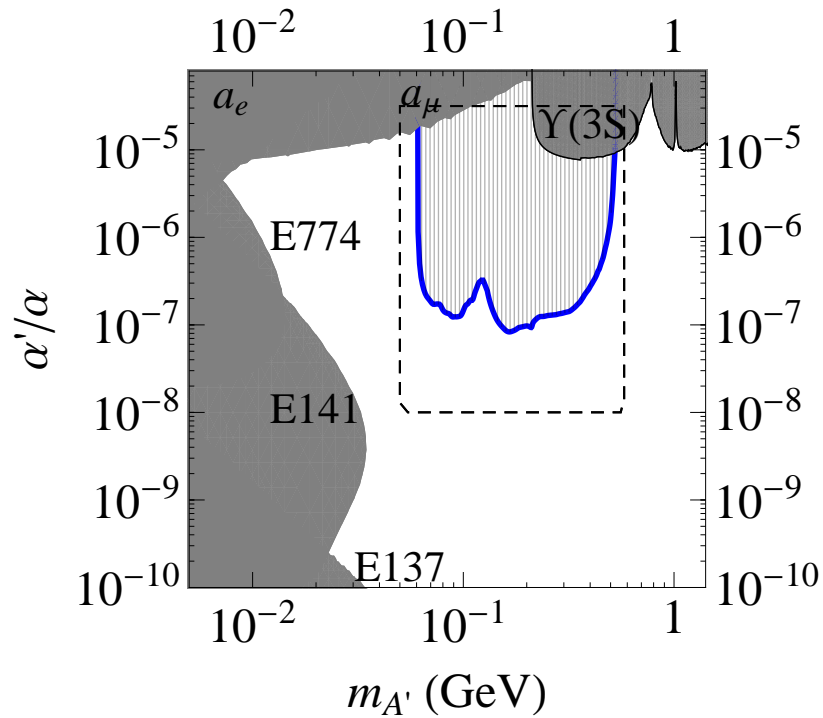


Figure 1: Anticipated 2σ sensitivity for the proposed experiment (thick blue line), with existing constraints on an A' from electron and muon anomalous magnetic moment measurements, a_e and a_μ (see [3]), the BaBar search for $\Upsilon(3S) \rightarrow \gamma\mu^+\mu^-$ [4], and three beam dump experiments, E137, E141, and E774 [5, 6, 7] (see [8]). The a_μ and $\Upsilon(3S)$ limits assume equal-strength couplings to electrons and muons. The gray dashed line indicates the scale used for other plots in this paper. Note that the sensitivity curve is the combined sensitivity from runs at four different energy settings (see Figure 24) – the decrease in the sensitivity between 100 – 200 MeV could be removed by choosing a different setting.

to a new gauge boson A' , which is quite poorly constrained for small g' (see Figure 1)[8]. Similar couplings between the A' and other Standard Model fermions are also allowed, with relations between their couplings (anomaly cancellation) required for the A' gauge symmetry to be quantum-mechanically consistent. For example, the A' can couple only to electrons and muons, with opposite charges $g'_e = -g'_\mu$ (a $U(1)_{e-\mu}$ boson), or can have couplings proportional to the electromagnetic charges of each fermion, $g_i = \epsilon e q_i$.

In the second case, the A' coupling to Standard Model matter can be *induced* by ordinary electromagnetic interactions, through the kinetic mixing interaction proposed by Holdom [1],

$$\delta\mathcal{L} = \frac{\epsilon_Y}{2} F'_{\mu\nu} F_Y^{\mu\nu}, \quad (2)$$

where $F'_{\mu\nu} = \partial_\mu A'_\nu - \partial_\nu A'_\mu$ is the field strength of the A' gauge boson, and similarly $F_Y^{\mu\nu}$ is the hypercharge field strength. This effect is generic, ensures that the A' interactions respect parity, and (as we discuss below) naturally produces small g' and A' masses near the GeV scale. This mixing is equivalent in low-energy interactions to assigning a charge $\epsilon e q_i$ to Standard Model particles of electromagnetic charge q_i , where $\epsilon = \epsilon_Y / (\cos \theta_W)$ and θ_W is the Weinberg mixing angle. The A' couplings to neutrinos and parity-violating couplings are negligible compared to Z -mediated effects (see e.g. [14]).

As noted in [1], a new gauge boson A' that does not couple to Standard Model matter at a classical level can still couple through quantum-mechanical corrections. For example, loops of any particle X that couples to both the A' and Standard Model hypercharge generates mixing of the form (2), with

$$\epsilon \sim 10^{-3} - 10^{-2} \quad (\alpha'/\alpha \sim 10^{-6} - 10^{-4}). \quad (3)$$

These quantum effects are significant regardless of the mass m_X of the particle in question, which could be well above the TeV scale (or even at the Planck scale) and thus evade detection.

Smaller ϵ are expected if nature has enhanced symmetry at high energies. For example, it has been conjectured that the strong and electroweak gauge groups of the Standard Model are embedded in a grand unified theory (GUT) with gauge group $SU(5)$ or larger that is broken spontaneously at a high scale $M_G \approx 10^{16}$ GeV. In this case the mixing (2) is suppressed,

$$\epsilon_{GUT} \sim \frac{\alpha_i^2}{16\pi^2} \ln(M_G/M_X) \sim 10^{-3} - 10^{-5}, \quad (4)$$

where α_i are gauge couplings. ϵ of this size leads to effective couplings

$$\alpha'/\alpha \sim 10^{-6} - 10^{-8}. \quad (5)$$

As shown in Figure 1, *no experiment to date has probed the range of ϵ expected in grand unified theories for $m_{A'} \gtrsim 50$ MeV.*

An A' mass near but beneath the weak scale is particularly well-motivated, as $U(1)'$ symmetry-breaking and the resulting A' mass may be determined by the same physics that generates the W and Z masses [15]. The best candidate for the origin of the weak scale is low-energy supersymmetry. In this case, the A' can naturally acquire mass suppressed by a loop factor or by $\sqrt{\epsilon}$ compared to the weak scale, leading to MeV to GeV-scale A'

masses [9, 15, 16, 17, 18, 14]. In supersymmetric models, the gauge kinetic mixing (2) is accompanied by quartic interactions

$$\delta\mathcal{L} \sim \frac{\epsilon_Y}{4} g_Y g_D |\phi_D|^2 |h|^2, \quad (6)$$

between the Standard Model Higgs doublet h and any scalar ϕ_D charged under $U(1)'$, where g_Y and g_D are the gauge couplings of Standard Model hypercharge and the A' coupling to ϕ_D , respectively. Electroweak symmetry breaking gives h a weak-scale vacuum expectation value, so that (6) generates a mass term for ϕ_D . For positively charged ϕ_D , and sufficiently small bare mass, this mass term is negative and triggers $U(1)'$ breaking by the Higgs mechanism. The resulting induced mass for the A' is

$$m_{A'} \sim \sqrt{\epsilon} \sqrt{\frac{g_D g_Y}{g_2^2}} m_W \sim \text{MeV-GeV}, \quad (7)$$

where g_2 is Standard Model $SU(2)_L$ gauge coupling and m_W is the W-boson mass. The resulting mass is precisely in the 50 – 1000 MeV range targeted by this experiment. Given our ϵ sensitivity, we expect to probe the portion of this parameter space with small g_D . For example, for $g_D \sim 0.04$ and $\epsilon \sim 5 \times 10^{-4}$ ($\alpha'/\alpha \sim 2.5 \times 10^{-7}$), we have $m_{A'} \sim 400$ MeV, which can definitively be probed by the proposed experiment. Note that the mechanism of $U(1)'$ breaking above does not rely on supersymmetry, as any quartic interaction of the form (6), with arbitrary coupling, can transmit electro-weak masses to the A' . Thus, the mass relation (7) should not be interpreted too literally.

We stress that the mass of the A' breaks any apparent symmetry between it and the photon: though Standard Model particles have induced ϵ -suppressed charges under the A' , any new matter charged under the A' would *not* have any effective coupling to the photon, and would have gone undetected.

The Hall A HRS is ideally suited to explore the A' parameter space. An electron beam scattering on a high- Z target such as Tungsten will produce A' 's through bremsstrahlung reactions with a cross-section

$$\sigma_{A'} \sim 100 \text{ pb} \left(\frac{\epsilon}{10^{-4}} \right)^2 \left(\frac{100 \text{ MeV}}{m_{A'}} \right)^2, \quad (8)$$

several orders of magnitude larger than in colliding electron and hadron beams [19]. The A' can decay to electrons, and is therefore visible as a narrow resonance in the trident e^+e^- mass spectrum.

Such a new gauge boson would constitute the first discovery of a new gauge force since the observation of Z -mediated neutral currents. Besides the obvious physical interest of a fifth force, the A' like the Z could open up a new “sector” of light, weakly coupled particles whose spectrum and properties could be measured in fixed-target experiments and flavor factories. The A' sector would provide a new laboratory for many physical questions, and would be revealing precisely because its interactions with Standard Model particles are so weak. In particular, if nature is approximately supersymmetric near the TeV scale, the mass scale of supersymmetry breaking for the A' sector is naturally suppressed by ϵ times gauge couplings. In this case, supersymmetry could be studied easily in the A' sector, and possibly even discovered there by relatively low-energy experiments before Standard Model superpartners are seen at colliders.

2.2 Motivation for an A' from Dark Matter

Dark matter interpretations of recent astrophysical and terrestrial anomalies provide an urgent impetus to search for A' 's in the mass range 50 MeV – 1 GeV, with a coupling $\epsilon \sim 10^{-4} - 10^{-2}$.

The concordance model of big bang cosmology — the “Lambda Cold Dark Matter” (Λ CDM) model — explains all observations of the cosmic microwave background, large scale structure formation, and supernovae. This model suggests that Standard Model particles make up only about 4% of the energy density in the Universe, while “dark energy” and “dark matter” make up 74% and 22%, respectively, of the Universe’s energy density. The concordance model does not require dark matter to have any new interactions beyond gravity with Standard Model particles. However, an intriguing theoretical observation, dubbed the *WIMP miracle*, suggests that dark matter *does* have new interactions. In particular, if dark matter consists of ~ 10 GeV to 10 TeV particles interacting via the electroweak force (“weakly interacting massive particles” or “WIMPs”), they would automatically have the right relic abundance observed today.

In addition to the WIMP miracle, evidence from cosmic-ray data, from balloon-borne instruments and satellites, and the terrestrial direct dark matter detection experiment DAMA/LIBRA and CoGeNT suggest that dark matter interacts with ordinary matter *not* just gravitationally. While the WIMP miracle hints that dark matter is charged under the Standard Model electroweak force, we will see that *these observations are suggestive that dark matter interacts with ordinary matter through a new force, mediated by a new 50 MeV – 1 GeV mass gauge boson*. In addition to explaining any or all of these observations, dark matter charged under this new force automatically has the correct thermal relic abundance observed today by virtue of its interactions via the new force carrier, reproducing the success of the WIMP dark matter hypothesis.

The satellites PAMELA [20] and Fermi [21], the balloon-borne detector ATIC [22], the ground-based telescope HESS [23, 24], as well as other experiments, observe an excess in the cosmic-ray flux of electrons and/or positrons above backgrounds expected from normal astrophysical processes. While this excess may be due to nearby pulsars or supernova remnants, a plausible origin is dark matter annihilation or decay. However, two features of these observations are incompatible with annihilation of ordinary thermal WIMP dark matter. They instead provide impressive evidence that dark matter is charged under a new $U(1)'$ and annihilating into the A' , which decays directly into electrons and positrons, or into muons that decay into electrons and positrons, see Figure 2 (left) (see e.g. [25, 26, 27, 28, 29, 30, 31, 32]). These two features are:

- The annihilation cross-section required to explain the signal is 50-1000 times larger than the thermal freeze-out cross-section for an ordinary WIMP that is needed to reproduce the observed dark matter relic density. This can be explained if dark matter interacts with a new long range force mediated by an $\mathcal{O}(\text{GeV})$ mass gauge boson, which allows the dark matter annihilation cross-section ($\langle\sigma v\rangle$) to be enhanced at low dark matter velocities, i.e. $\langle\sigma v\rangle \propto 1/v$. In this case, in the early Universe when the dark matter velocity was high ($\sim 0.3c$), the annihilation cross-section that determines the relic abundance can naturally be the same as that of an ordinary WIMP and reproduce the WIMP miracle. However, in the Milky Way halo now, the dark matter has a much lower velocity ($v \sim 10^{-3}c$), leading to a large increase in the annihilation cross-section

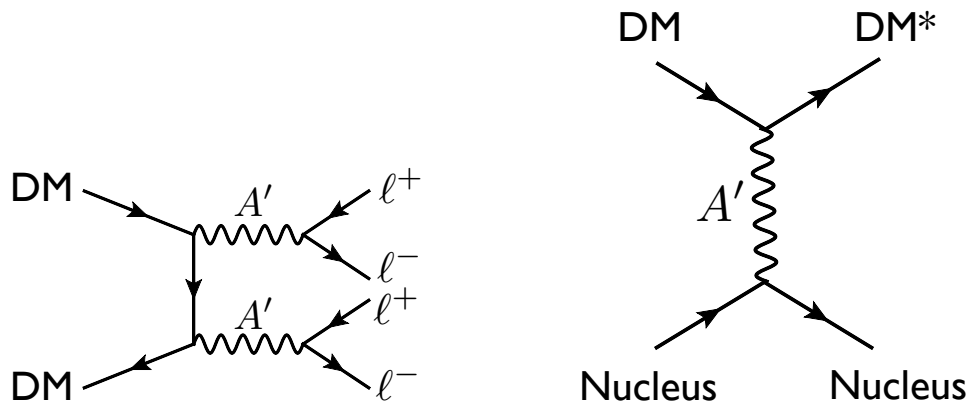


Figure 2: **Left:** Dark matter annihilation into the dark photon A' , which decays into charged leptons such as electrons and/or muons, can explain the cosmic-ray electron and/or positron excesses seen by PAMELA, Fermi, ATIC, HESS, and other experiments. **Right:** Dark matter scattering into an excited state off nuclei through A' exchange in direct dark matter detection experiments can explain the annual modulation signal observed by DAMA/LIBRA, and the null results of other direct detection experiments.

that is required to explain the cosmic-ray data. The enhancement at low velocities through a new long-range force is very well known and called the Sommerfeld effect [33]. We refer the reader to [34] for a recent detailed discussion.

- The PAMELA satellite did *not* see an anti-proton excess [35], which strongly suggests that dark matter annihilation is dominantly producing leptons, and not baryons. If dark matter is interacting via a $\mathcal{O}(\text{GeV})$ mass force particle in order to have a large annihilation rate via the Sommerfeld mechanism, then annihilations into the force carrier automatically fail to produce any baryons. Kinematically, the force carriers cannot decay into baryons, and are instead forced to decay into the lighter charged leptons. Thus, the annihilation products of dark matter would automatically be leptonic.

To explain the additional sources of evidence for a new GeV scale force, we briefly summarize the consequence for dark matter mass spectra that follow from dark matter carrying a charge under a new force. If dark matter is charged under a non-Abelian force that acquires mass, then radiative effects can split all components of the dark matter with size, $\delta \sim \alpha_D \Delta m_{W_D}$, where α_D is the non-Abelian fine structure constant and Δm_{W_D} is the splitting of gauge boson masses [25]. Typically, these splittings are $\Delta m_{W_D} \sim \alpha_D m_{W_D} \sim 1 - 10 \text{ MeV}$ for $m_{W_D} \sim 1 \text{ GeV}$ [25]. Thus, $\delta \sim 100 \text{ keV}$ for $\alpha_D \sim 10^{-2}$. These splittings are completely analogous to the splittings that arise between the π^\pm and π^0 from Standard Model SU(2) breaking. If instead a non-Abelian force confines at a scale $\Lambda_D \sim \text{GeV}$, then a heavy-flavor meson can be cosmologically long-lived and thus a dark matter candidate [36]. Hyperfine interactions can naturally induce $\sim 100 \text{ keV}$ splittings of the dark matter particles in this case. We emphasize that the GeV scale force carrier particles mediate quantum corrections that generate the 100 keV and 1-10 MeV splittings of dark matter states [25, 37, 38, 36].

When mass splittings arise, A' mediated interactions of dark matter with ordinary matter as well as dark matter self-interactions are dominated by inelastic collisions [25]. The direct dark matter detection experiment DAMA/LIBRA as well as the INTEGRAL telescope provide intriguing evidence for such interactions. The DAMA/NaI [39] and DAMA/LIBRA [40] experiments have reported an annual modulation signal over nearly eleven years of operation with more than 8σ significance. Modulation is expected because the Earth's velocity with respect to the dark matter halo varies as the Earth moves around the sun, and the phase of the observed modulation is consistent with this origin. A simple hypothesis that explains the spectrum and magnitude of the signal, and reconciles it with the null results of other experiments, is that dark matter-nucleus scattering is dominated by an inelastic process,

$$\chi N \rightarrow \chi^* N, \quad (9)$$

in which the dark matter χ scatters off a nucleus N into an excited state χ^* with mass splitting $\delta \approx 100$ keV [37]. The kinematics of these reactions is also remarkably consistent with all the distinctive properties of the nuclear recoil spectrum reported by DAMA/LIBRA. In addition, the INTEGRAL telescope [41] has reported a 511keV photon signal near the galactic center, indicating a new source of ~ 1 -10 MeV electrons and positrons. This excess could be explained by collisions of $\mathcal{O}(100 \text{ GeV}-1 \text{ TeV})$ mass dark matter into $\mathcal{O}(\text{MeV})$ excited states in the galaxy [42] — dark matter excited by scattering decays back to the ground state by emitting a soft e^+e^- pair. The 511keV excess then arises from the subsequent annihilation of the produced positrons.

The above dark matter related anomalies are thus consistent with 100 GeV - 1 TeV mass dark matter interacting with ordinary matter through an A' . By itself, the DAMA/LIBRA anomaly can also be explained with light dark matter, a 5-10 GeV dark matter particle scattering off nuclei through A exchange. Such a low dark matter mass cannot explain the cosmic-ray anomalies, but is motivated instead by another direct dark matter detection experiment, CoGeNT, that has recently reported an anomaly. The CoGeNT collaboration reported about 100 events from an unknown source in a low-threshold, high-resolution Ge detector [43]. These events are consistent with a 5-10 GeV dark matter particle scattering off the Germanium nuclei in the CoGeNT detector [44]. The required dark matter mass and scattering cross-section are intriguingly close to the values needed to also explain the DAMA/LIBRA annual modulation signal.

The Standard Model particles that are usually invoked to explain dark matter scattering off nuclei are the Higgs boson and the Z -boson. However, the Higgs boson couples only weakly to nuclei and typically generates scattering cross-sections $\lesssim 10^{-43} \text{ cm}^2$, which is much smaller than the required cross-section ($\sim 10^{-40} \text{ cm}^2$) to explain DAMA/LIBRA and CoGeNT. The Z -boson can provide a cross-section of the right size, but measurements of the invisible width of the Z at LEP tightly constrain the coupling between dark matter and the Z -boson (since the Z is kinematically allowed to decay into 5-10 GeV dark matter particle if they couple to each other). An A' mediating the scattering, however, can easily produce the required cross-section and satisfy all constraints.

Remarkably, it is even possible to build models in which both the DAMA/LIBRA and CoGeNT signals and the cosmic-ray anomalies are naturally explained by dark matter coupling to an A' [45]. For this we need two dark matter components: the dominant dark matter component consists of a TeV-scale particle annihilating or decaying to an A' , which in turn decays to charged leptons to explain the cosmic-ray anomalies; a subdominant ($< 1\%$) com-

ponent consists of a 5 GeV particle that scatters off the nuclei in the DAMA/LIBRA and CoGeNT detectors via A' exchange. The required cross-section can be naturally obtained in a supersymmetric model.

In addition to the various dark matter anomalies, the existence of an A' may also help explain various other particle physics anomalies [3] such as the anomalous magnetic moment of the muon ($a_\mu \equiv (g - 2)_\mu$) [46]. The A' mass and coupling suggested by this anomaly lies close to the a_μ bound shown in, for example, Fig. 1. The APEX experiment will probe a large part of this parameter space.

While these experimental hints provide an urgent motivation to look for an A' , it is important to emphasize the value of these searches in general. There has never been a systematic search for new GeV-scale force carriers that are weakly coupled to Standard Model particles. Nothing forbids their existence, and their discovery would have profound implications for our understanding of nature. A relatively simple experiment using the facilities available in Hall A at Jefferson Laboratory will probe a large and interesting range of A' masses and couplings.

2.3 Existing constraints

Constraints on new A' 's that decay to e^+e^- and the search reach of an experiment using the spectrometers of Hall A at Jefferson Laboratory are summarized in Figure 1. Shown are constraints from electron and muon anomalous magnetic moment measurements, a_e and a_μ [3], the BaBar search for $\Upsilon(3S) \rightarrow \gamma A' \rightarrow \gamma \mu^+ \mu^-$ [19], three beam dump experiments, E137, E141, and E774 [8]. The constraints from a_μ and the BaBar search assume that the A' couples to muons — this is the case, for example, if it mixes with the photon. If it only couples to electrons, then the constraints on α'/α and $m_{A'}$ in the region to which the proposed experiment is sensitive are weaker than $\alpha'/\alpha \lesssim 10^{-4}$.

We refer the reader to [8, 3] for details on existing constraints. Here, we briefly review the constraint on $e^+e^- \rightarrow \gamma A' \rightarrow \gamma \mu^+ \mu^-$ derived from the BaBar search [47]. If the A' couples to both electrons and muons, this is the most relevant constraint in the region probed by the proposed experiment. The analysis of [47] was in fact a search for $\Upsilon(3S)$ decays into a pseudoscalar a , $\Upsilon(3S) \rightarrow \gamma a \rightarrow \gamma \mu^+ \mu^-$, but can be interpreted as a limit on A' production because the final states are identical. Using $\mathcal{L}_{\text{int}} \sim 30 \text{ fb}^{-1}$ of data containing $\sim 122 \times 10^6$ $\Upsilon(3S)$ events, a 90% C.L. upper limit of roughly $(1 - 4) \times 10^{-6}$ on the $\gamma \mu^+ \mu^-$ branching fraction was found for $m_{A'} \sim 2m_\mu - 1 \text{ GeV}$. This search would thus be sensitive to about $\sim 100 - 500$ events with $e^+e^- \rightarrow \gamma A' \rightarrow \gamma \mu^+ \mu^-$. Requiring that $\sigma(e^+e^- \rightarrow \gamma A') \times BR(A' \rightarrow \mu^+ \mu^-) \times \mathcal{L}_{\text{int}} \lesssim 500$, where $BR(A' \rightarrow \mu^+ \mu^-) = 1/(2 + R(m_{A'}))$ for $m_{A'} > 2m_\mu$ with $R = \frac{\sigma(e^+e^- \rightarrow \text{hadrons}; E=m_{A'})}{\sigma(e^+e^- \rightarrow \mu^+ \mu^-; E=m_{A'})}$, and rescaling the resulting constraint to represent a 95% C.L. upper bound, we find the constraint depicted in Figure 1. For $m_{A'} \gtrsim 2m_\mu$, this requires $\alpha'/\alpha \gtrsim 10^{-5}$, while the constraint weakens at higher masses, especially near the ρ -resonance.

We caution that systematic uncertainties in the A' limit beyond those quoted in [47] may slightly weaken the resulting limit, which should therefore be taken as a rough approximation unless further analysis is done. First, A' production in B-factories is more forward-peaked than the $\Upsilon(3S)$ decay mode considered in [47], so that the signal acceptance is more uncertain. In addition, background distributions in [47] are derived from smooth polynomial fits to data collected on the $\Upsilon(4S)$ resonance, which is assumed to contain no signal. This assumption is not correct for A' production, though the resulting systematic effects are expected to

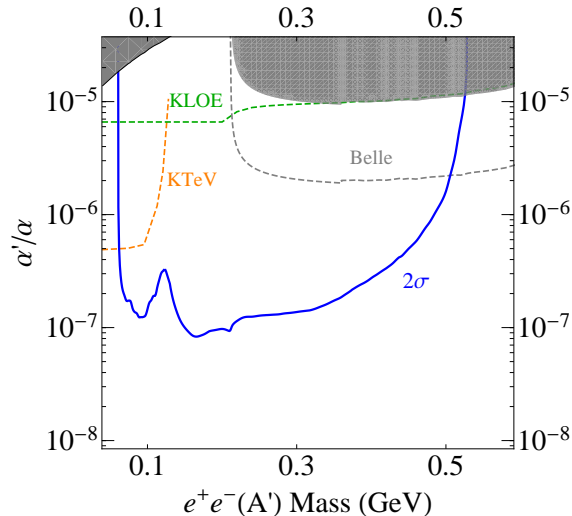


Figure 3: The 2σ sensitivity of the proposed experiment (blue line), compared with current limits and estimated potential 2σ sensitivity for A' searches in existing data (dashed lines), assuming optimal sensitivity as described in the text. From left to right: KTeV $\pi^0 \rightarrow \gamma A' \rightarrow \gamma e^+e^-$ (orange dashed curve), KLOE $\phi \rightarrow \eta A' \rightarrow \eta e^+e^-$ (green dashed curve) and Belle $e^+e^- \rightarrow \gamma A' \rightarrow \gamma \mu^+\mu^-$ (gray dashed curve). Existing constraints are as in Figure 1.

be small.

2.4 Potential Improvements From Existing Data

Several past and current experiments have data that could be used to significantly improve current limits on α'/α , as discussed in [3, 48]. Here, we estimate the potential sensitivity of searches in three channels ($\pi^0 \rightarrow \gamma A' \rightarrow \gamma e^+e^-$, $\phi \rightarrow \eta A' \rightarrow \eta e^+e^-$, and $e^+e^- \rightarrow \gamma A' \rightarrow \gamma \mu^+\mu^-$), considering only the statistical uncertainties and irreducible backgrounds. These are likely overestimates, as we are unable to include either systematic uncertainties or significant instrumental backgrounds such as photon conversion in the detector volume.

BaBar, BELLE, and KTeV (E799-II) have produced and detected large numbers of neutral pions, of order 10^{10} , of which roughly 1% decay in the Dalitz mode $\pi^0 \rightarrow e^+e^-\gamma$. These experiments can search for the decay $\pi^0 \rightarrow \gamma A'$ induced by A' -photon kinetic mixing, which would appear as a narrow resonance over the continuum Dalitz decay background. KTeV has the largest π^0 sample, and its e^+e^- mass resolution can be approximated from the reported measurement of the $\pi^0 \rightarrow e^+e^-$ branching fraction [49] to be roughly 2 MeV. This paper also reports the measured mass distribution of Dalitz decays above 70 MeV, from which we estimate potential sensitivity to α'/α as small as 5×10^{-7} for $70 < m(e^+e^-) \lesssim 100$ MeV, as shown by the orange shaded region in Figure 3.

Similarly, KLOE can search for the decay $\phi \rightarrow \eta A'$, likewise induced by A' kinetic mixing with the photon, in a sample of 10^{10} ϕ 's. An analysis of this data is ongoing [50]. We have taken the blue dashed curve in Figure 3 from [48], which assumes that mass resolution σ_m is dominated by KLOE's 0.4% momentum resolution. We have adjusted the contours from [48] to determine a 2σ contour and enlarge the bin width used to determine signal significance from σ_m in [48] to $2.5\sigma_m$). Above the muon threshold, ϕ decays are not competitive with

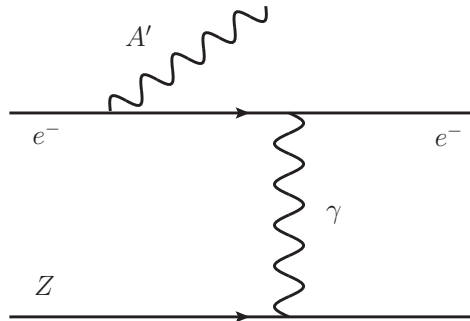


Figure 4: A' production by bremsstrahlung off an incoming electron scattering off protons in a target with atomic number Z .

B-factory continuum production.

In addition, BaBar and Belle can search for the continuum production mode $e^+e^- \rightarrow \gamma A' \rightarrow \gamma \mu^+ \mu^-$ in their full datasets. For example, an analysis of the Belle $\Upsilon(4S)$ data set would increase statistics by a factor of ~ 24 relative to the BaBar $\Upsilon(3S)$ search that we have interpreted as a limit above. We have derived the expected sensitivity (shown as a black dashed line in Figure 3) simply by scaling the $\Upsilon(3S)$ estimated reach by $\sqrt{24}$. These searches have not been extended below the muon threshold because of large conversion backgrounds.

3 The production of an A' in fixed target collisions

A' particles are generated in electron collisions on a fixed target by a process analogous to ordinary photon bremsstrahlung, see Figure 4. This can be reliably estimated in the Weizsäcker-Williams approximation (see [8, 51, 52, 53]). When the incoming electron has energy E_0 , the differential cross-section to produce an A' of mass $m_{A'}$ with energy $E_{A'} \equiv xE_0$ is

$$\frac{d\sigma}{dx d\cos\theta_{A'}} \approx \frac{8Z^2\alpha^3\epsilon^2 E_0^2 x}{U^2} \tilde{\chi} \times \left[\left(1 - x + \frac{x^2}{2}\right) - \frac{x(1-x)m_{A'}^2 (E_0^2 x \theta_{A'}^2)}{U^2} \right] \quad (10)$$

where Z is the atomic number of the target atoms, $\alpha \simeq 1/137$, $\theta_{A'}$ is the angle in the lab frame between the emitted A' and the incoming electron,

$$U(x, \theta_{A'}) = E_0^2 x \theta_{A'}^2 + m_{A'}^2 \frac{1-x}{x} + m_e^2 x \quad (11)$$

is the virtuality of the intermediate electron in initial-state bremsstrahlung, and $\tilde{\chi} \sim 0.1 - 10$ is the Weizsäcker-Williams effective photon flux, with an overall factor of Z^2 removed. The form of $\tilde{\chi}$ and its dependence on the A' mass, beam energy, and target nucleus are discussed in Appendix A. The above results are valid for

$$m_e \ll m_{A'} \ll E_0, \quad x \theta_{A'}^2 \ll 1. \quad (12)$$

For $m_{A'} \gg m_e$, the angular integration gives

$$\frac{d\sigma}{dx} \approx \frac{8Z^2\alpha^3\epsilon^2 x}{m_{A'}^2} \left(1 + \frac{x^2}{3(1-x)}\right) \tilde{\chi}. \quad (13)$$

The rate and kinematics of A' radiation differ from massless bremsstrahlung in several important ways:

Rate: The total A' production rate is controlled by $\frac{\alpha^3 \epsilon^2}{m_{A'}^2}$. Therefore, it is suppressed relative

to photon bremsstrahlung by $\sim \epsilon^2 \frac{m_e^2}{m_{A'}^2}$. Additional suppression from small $\tilde{\chi}$ occurs for large $m_{A'}$ or small E_0 .

Angle: A' emission is dominated at angles $\theta_{A'}$ such that $U(x, \theta_{A'}) \lesssim 2U(x, 0)$ (beyond this point, wide-angle emission falls as $1/\theta_{A'}^4$). For x near its median value, the cutoff emission angle is

$$\theta_{A' \text{ max}} \sim \max \left(\frac{\sqrt{m_{A'} m_e}}{E_0}, \frac{m_{A'}^{3/2}}{E_0^{3/2}} \right), \quad (14)$$

which is parametrically smaller than the opening angle of the A' decay products, $\sim m_{A'}/E_0$. Although this opening angle is small, the backgrounds mimicking the signal (discussed in Section 6) dominate at even smaller angles.

Energy: A' bremsstrahlung is sharply peaked at $x \approx 1$, where $U(x, 0)$ is minimized. When an A' is produced, it carries nearly the entire beam energy — in fact the median value of $(1 - x)$ is $\sim \max \left(\frac{m_e}{m_{A'}}, \frac{m_{A'}}{E_0} \right)$.

The latter two properties are quite important in improving signal significance, and are discussed further in Section 6.

Assuming the A' decays into Standard Model particles rather than exotics, its boosted lifetime is

$$\ell_0 \equiv \gamma c \tau \simeq \frac{3E_{A'}}{N_{\text{eff}} m_{A'}^2 \alpha \epsilon^2} \simeq \frac{0.8 \text{ cm}}{N_{\text{eff}}} \left(\frac{E_0}{10 \text{ GeV}} \right) \left(\frac{10^{-4}}{\epsilon} \right)^2 \left(\frac{100 \text{ MeV}}{m_{A'}} \right)^2, \quad (15)$$

where we have neglected phase-space corrections, and N_{eff} counts the number of available decay products. If the A' couples only to electrons, $N_{\text{eff}} = 1$. If the A' mixes kinetically with the photon, then $N_{\text{eff}} = 1$ for $m_{A'} < 2m_\mu$ when only $A' \rightarrow e^+e^-$ decays are possible, and $2 + R(m_{A'})$ for $m_{A'} \geq 2m_\mu$, where $R = \frac{\sigma(e^+e^- \rightarrow \text{hadrons}; E=m_{A'})}{\sigma(e^+e^- \rightarrow \mu^+\mu^-; E=m_{A'})}$ [54]. For the ranges of ϵ and $m_{A'}$ probed by this experiment, the mean decay length $\ell_0 \lesssim 250 \mu\text{m}$ is not significant, but the ability to cleanly reconstruct vertices displaced forward by a few cm would open up sensitivity to considerably lower values of ϵ .

The total number of A' produced when N_e electrons scatter in a target of $T \ll 1$ radiation lengths is

$$N \sim N_e \frac{N_0 X_0}{A} T \frac{Z^2 \alpha^3 \epsilon^2}{m_{A'}^2} \tilde{\chi} \sim N_e \mathcal{C} T \epsilon^2 \frac{m_e^2}{m_{A'}^2}, \quad (16)$$

where X_0 is the radiation length of the target in g/cm^2 , $N_0 \simeq 6 \times 10^{23} \text{ mole}^{-1}$ is Avogadro's number, and A is the target atomic mass in g/mole . The numerical factor $\mathcal{C} \approx 5$ is logarithmically dependent on the choice of nucleus (at least in the range of masses where the form-factor is only slowly varying) and on $m_{A'}$, because, roughly, $X_0 \propto \frac{A}{Z^2}$ (see [8] and [54]). For a Coulomb of incident electrons, the total number of A' 's produced is very roughly given by

$$\frac{N}{\mathcal{C}} \sim 10^5 \tilde{\chi} \left(\frac{T}{0.1} \right) \left(\frac{\epsilon}{10^{-4}} \right)^2 \left(\frac{100 \text{ MeV}}{m_{A'}} \right)^2. \quad (17)$$

The spectrometer efficiency can be estimated from Monte Carlo simulation of the signal, discussed in Section 5. It is quite low, but of course depends on the precise spectrometer settings. For example, for $m_{A'} = 200$ MeV, $E_0 = 3.056$ GeV, an angular acceptance window of $\theta_x = 0.055 - 0.102$ mrad and $|\theta_y| \leq 0.047$ mrad (corresponding to an HRS central angle of 4.5°) and a momentum acceptance of $E = 1.452 - 1.573$ GeV for both the positron and one of the electrons, gives a spectrometer efficiency of $\sim 0.14\%$.

4 Experimental setup

The proposed experiment will study e^+e^- production off an electron beam incident on a high- Z target as illustrated in Figure 5. The beam will pass through a target consisting of narrow strips of tungsten foil, with total thickness between 0.5% and 10% X_0 for each running configuration. The beam will be rastered in both directions: horizontally by ± 0.25 mm and vertically by ± 2.5 mm. The e^+e^- pair components will be detected in the HRS spectrometers. The detector package in each HRS includes two vertical drift chambers (VDC), the single-PMT trigger scintillator counter (S0), the Gas Cherenkov counter, the segmented high-resolution scintillator hodoscope, and the double-layer lead-glass shower counter.

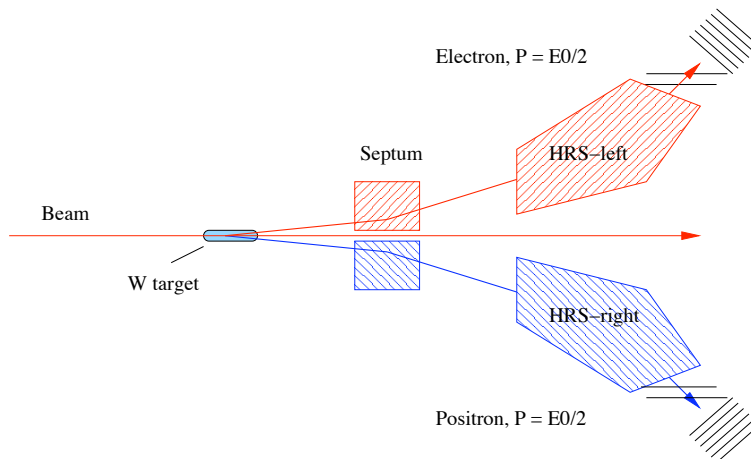


Figure 5: The layout of the experimental setup.

4.1 Concept of the experiment

The experiment will measure the invariant mass spectrum of e^+e^- pairs produced by an incident beam of electrons on a tungsten target, in four kinematic settings. The search for an A' peak will be done in the mass range from ~ 65 MeV to 525 MeV. The experiment will be performed in Hall A at JLab using two high-resolution spectrometers [55] together with a septa magnet constructed for the PREX experiment [2]. The electron beam with a current of $\lesssim 80 \mu A$ will be incident on a solid target located on a standard target ladder in a standard scattering chamber. The target will be made of a set of 10 tungsten strips strung vertically with their planes orthogonal to the beam direction. The beam will be rastered by ± 0.25 mm in the horizontal and ± 2.5 mm in the vertical direction.

The electron will be detected in the left HRS (HRS-L) and the positron will be detected in the right HRS (HRS-R). The trigger will be formed by a coincidence of two signals from the S2m counters of the two arms with a signal from the gas Cherenkov counter of the HRS-R (positive polarity arm). A timing window of 20 ns will be used for the first coincidence and 40 ns for the second coincidence. The resulting signal will be used as a primary trigger of DAQ.

An additional logic will be arranged for a coincidence in the S2m counters in the HRS-L and HRS-R. This second type of trigger will be prescaled by a factor of 200 for DAQ. Single-arm triggers using the S0 counters will be used to calibrate and adjust the delays for individual PMTs in the S2m and the gas Cherenkov counters.

4.2 The multi-foil target

Before discussing the target in detail, we discuss the physics and design demands of the APEX target system:

- APEX requires the best possible mass resolution, which means that we must minimize the impact of multiple scattering of electron/positron pairs in the target material. On the other hand, we need a fairly thick overall production target to maximize statistics.
- APEX also requires a wide and uniform coverage in invariant mass. This suggests that we use a target that is elongated along the beam.
- With a long target system, optics calibration along the full length of the target requires a specialized optics target.
- Material selection for the production target is driven by the desire to achieve the highest possible ratio of signal to background, while keeping the background rate low enough so as not to overwhelm the triggering and data acquisition (DAQ) system. We therefore use high- Z targets, tungsten and tantalum, to maximize the production rate of electron/positron pairs as compared to pions.
- The signal is a coincident electron/positron pair. To minimize backgrounds from triggers on accidental coincidences, it is useful to have the target elements spread out along the beam direction so that vertex information can be used to reject a large portion of any accidental electron/positron pairs that appear in the triggered sample.
- We require reasonable material stability at high temperature, cooling of the target system, good alignment of the components, ability to survey the target system, ease of repair and changing target components, and low cost.

To meet the above goals at relatively low cost, APEX will use the standard Hall A scattering chamber as it is used by the PREX experiment. Provisions have been made to attach the APEX target system to the water-fall lifter. The target consists of four sections; an optics calibration target, an alignment target, an empty section, and a production target. The concept of the target is presented in Figure 6, and it has already been constructed by the SLAC group in the APEX collaboration.

As shown in Figure 6, the bottom target section is the production target. This consists of up to 10 tungsten or tantalum ribbons, each held in an aluminium holder specially designed

Overall Target System Layout

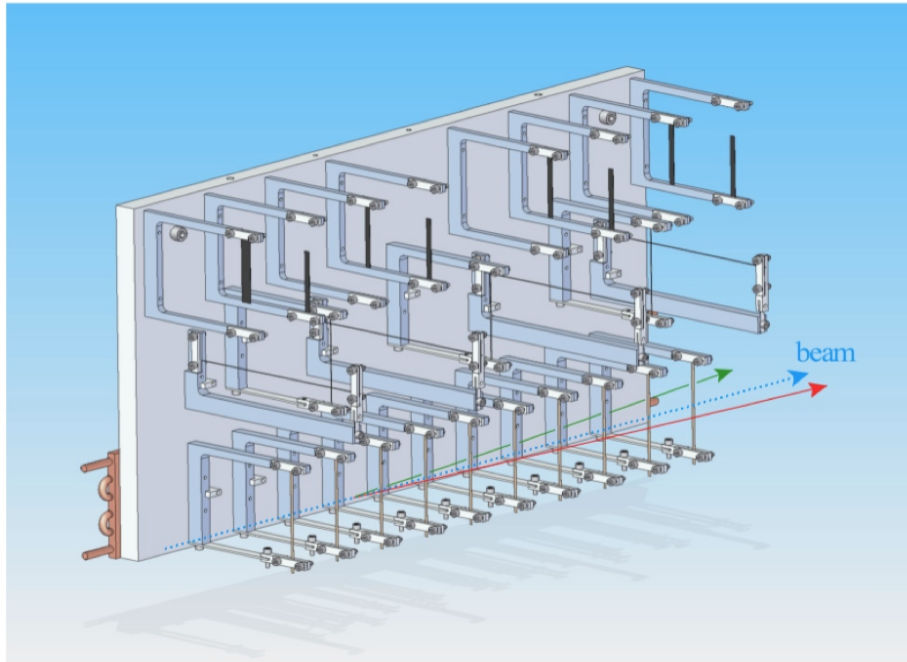


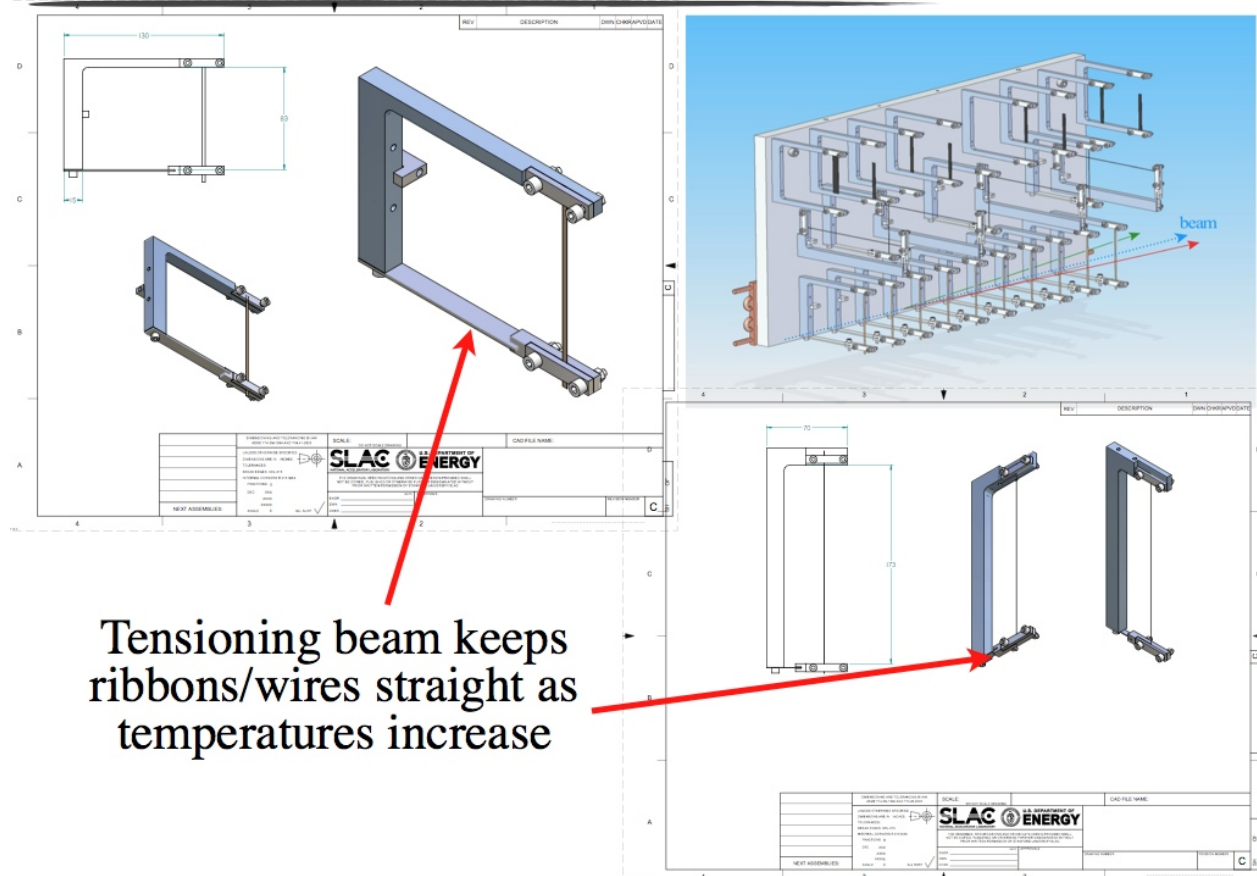
Figure 6: Overall layout of the APEX target system. The target consists of four sections from top to bottom; an optics calibration target, an alignment target, an empty section for beam studies, and a production target. Note that the target system is elongated along the beam line. The beam passes through all the production ribbons, while outgoing electron/positron pairs in the HRS acceptance only pass through one ribbon (shown with arrows).

to keep the ribbon at tension and prevent distortions at high temperature. The production target holders are shown in Figure 7. Each ribbon is 2.5 mm wide in order to accommodate raster of the beam. The currently purchased ribbons are 15 μm thick (or 0.43% of a radiation length), but ribbons of variable thicknesses can be purchased. The ribbon holders are spaced by 5.5 cm along the beam line. With this spacing, outgoing electron/positron pairs completely miss downstream ribbons when they are in the acceptance of the HRS. As a result, mass resolution is limited by the thickness of a single ribbon, while the beam electrons pass through all 10, thereby providing sufficient luminosity and minimal multiple-scattering effects.

The second section from the bottom in Figure 6 is an empty section used for beam tuning.

As shown in Figure 6, the second target section from the top is the beam-target alignment section. This consists of 4 horizontal and 3 vertical tungsten wires, each 100 μm in diameter. The wires are held by aluminum frames that keep the wires at tension to prevent sagging at high temperature. The alignment wire holders are shown in Figure 7. The 4 horizontal wires are arranged in 5 mm vertical steps at $-25, -10, 10, 25$ cm along the beam line. Likewise, the vertical wires are arranged in 2.5 mm horizontal steps at $-20, 0, 20$ cm along the beam line. With beam incident on the wires, beam-target alignment section will be used to precisely measure the beam direction relative to the alignment target. The alignment target system has in turn been surveyed relative to the full target system, so this provides a beam-target

Tensioned Holders



Tensioning beam keeps ribbons/wires straight as temperatures increase

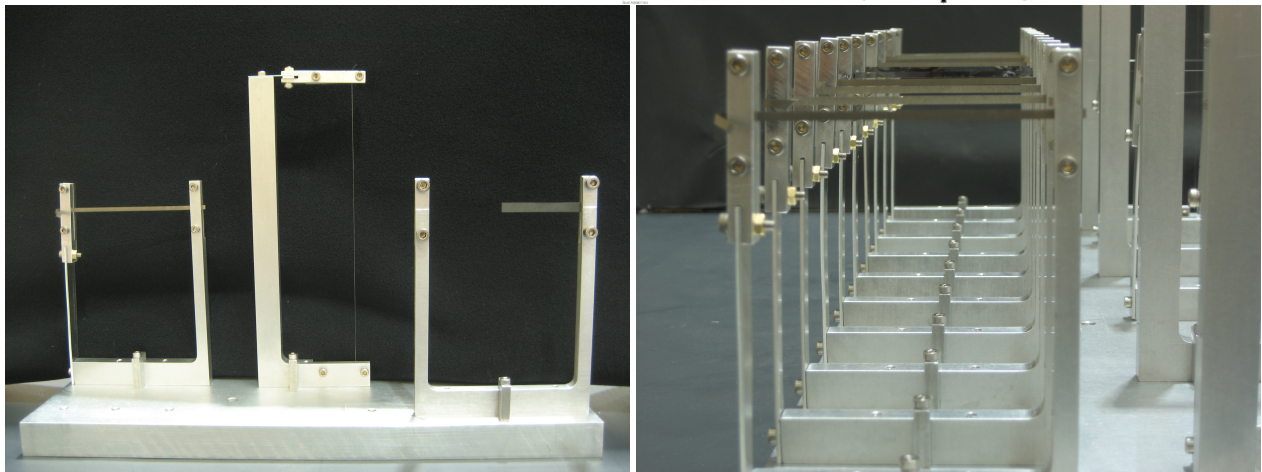


Figure 7: Top: schematic illustration of the production (left top) ribbon holder and beam-alignment wire holder (right top). On one side of each holder is a tensioning bar that is spring loaded. This keeps the ribbons or wires straight when the material is hot. Bottom left: A side view of all three target holders, where from left to right is the production ribbon, beam-alignment wire, and carbon foil optics holder. Bottom right: a front view showing all 10 production ribbons mounted in place.



Figure 8: Left photograph: Front view of the target sections, where from left to right the production, empty, alignment, and optics sections can be seen. Note the alternating orientations of the carbon foils in the optics section – this allows the beam to pass through two different sets of 4 foils (with 14 cm spacing along the beam line), or all 8 foils (with 7 cm spacing). Right photograph: front-side perspective showing the layout of the target sections.

alignment calibration for the entire APEX target system.

As shown in Figure 6, the top section is the optics calibration target. This consists of 8 carbon foils providing calibration points along the full length of the target system. The front foil is replaced with a BeO viewer. The foils are arranged so that the beam can pass through 4 foils at a time, or all 8 to provide an initial calibration with either 14 cm spacing along the beam line or 7 cm spacing.

Photographs of the nearly completed target system are shown in Figure 8. Figure 9 illustrates the impact of extending the APEX target system along the beam line. The maximum horizontal angular clearance is 11 degrees, with a 1 degree variation going into the HRS acceptance from front to back. For each energy setting of the APEX run plan, this provides a 50% increase in mass acceptance. The E06010 experiment used an elongated target system, and based on their results as well as measured HRS performance, we expect a transverse position resolution of ~ 1 mm. Consequently, we expect a ~ 1 cm resolution of vertices along the beam line. Given the 5.5 cm spacing of the production ribbons, we can use the anticipated vertex resolution to reduce any accidental coincidence backgrounds. This rejection power is not essential for the experimental performance, but will render coincidence backgrounds completely negligible.

For an electron beam of $80 \mu\text{A}$ on 10% X0 tungsten target, the maximum heat load is about 140 W. While this is an overestimate for all of the proposed run plan settings, the APEX target system includes up to 4 Lytron CP15 cold plates, installed on the back side of the primary aluminum mounting plate. The installation of these plates is shown in Figure 10. All of the target holders are aluminum so that heat is efficiently conducted into the aluminum mounting plate (over 1 cm thick). By running nitrogen gas in series (or parallel), we can provide sufficient heat removal to keep the mounting plate from reaching high temperatures.

Extended Mass Range Coverage

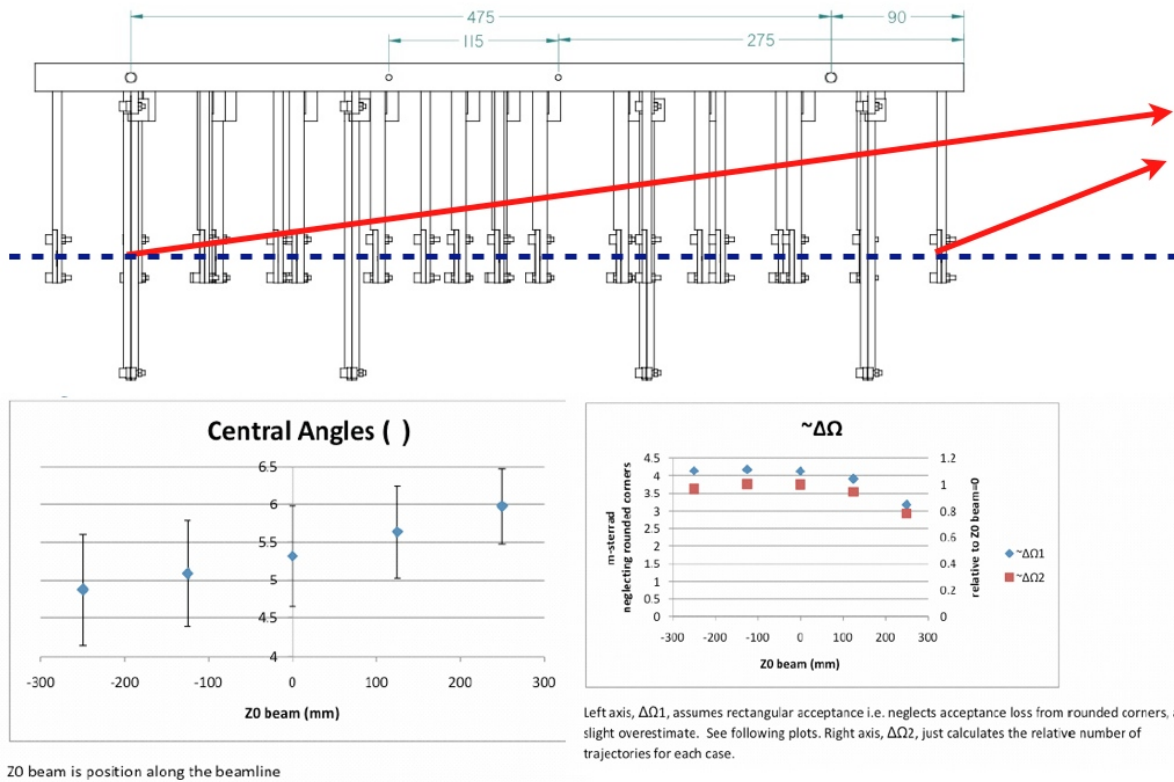
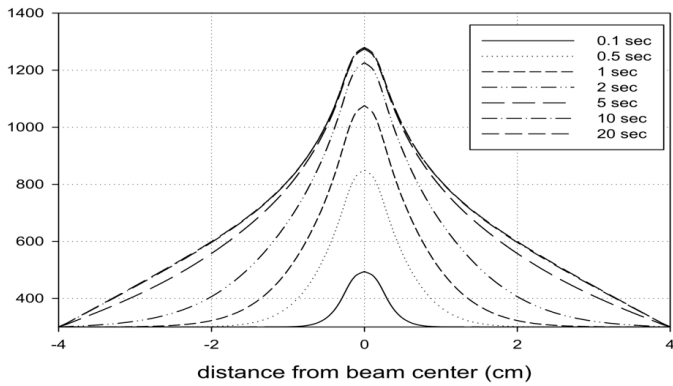


Figure 9: The bottom two plots show the results of MC study of the HRS angular acceptance with the septa magnet for different positions of the target along the beam direction. The top plot illustrates the impact of extending the APEX target system along the beam line. The maximum horizontal angular clearance is 11 degrees, with a 1 degree variation going into the HRS acceptance from front to back. For each energy setting of the APEX run plan, this provides a 50% increase in mass acceptance.

Also key is the thermal performance of the target material themselves. The SLAC group investigated the thermal behavior of the target elements to make sure that the anticipated heat loads would not melt the materials. Rastering of the beam (2 – 2.5 mm vertical and horizontal) will be required to prevent damage to the target materials at the highest current settings in the APEX run plan. Additionally, the tension bar in all the target holders was designed to account for the thermal expansion of the tungsten/tantalum ribbons and wires – the bar will keep the ribbons and wires straight at high temperature. Figure 10 shows a sample of results from numerical studies of the target system. Based on these investigations, we expect that heating of the ribbons will not be overly severe, elongation of the hot ribbons and wires is much smaller than the range of the tensioning beams, and the temperature profile of the ribbons is sufficiently smooth so that transverse stresses are not severe.

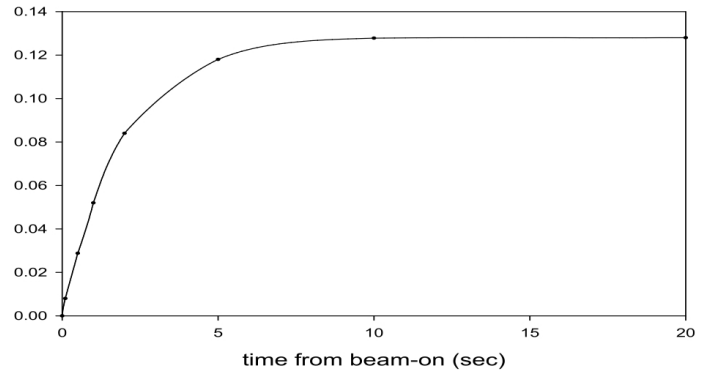
Tungsten Ribbon Temperature Profile

Tungsten foil, 15 microns thick \pm 4 cm tall.
Beam 40 μ A, dither \pm 2.5 mm high, beam sigma 0.4 mm,
beam just fills 2.5 mm wide ribbon



Tungsten Ribbon Thermal Expansion

Thermal expansion after beam turn on
of 80 mm long tungsten ribbon, 15 μ m thick.
Beam 40 μ A, 5 mm vertical dither, sigma 400 μ m.



Cooling Plates



- Up to 4 Lytron CP15 cold plates
- cooling supplied by nitrogen gas (in series or parallel)
- heat removal up to 200 Watts readily achievable

Figure 10: The bottom photograph shows the 4 Lytron CP15 cold plates attached to the target system mounting plate. Top left: the temperature profile of the tungsten production ribbons overlaid at various times. Top right: the thermal expansion fraction of the tungsten ribbons in beam relative to cold.

4.3 The room temperature septum magnet

The septum magnet (see Figure 11) was recently constructed and used in the PREX experiment with a $100 \mu\text{A}$ beam and a thick Pb target. This magnet allows one to change the direction of the field independently in the apertures for the two spectrometers.

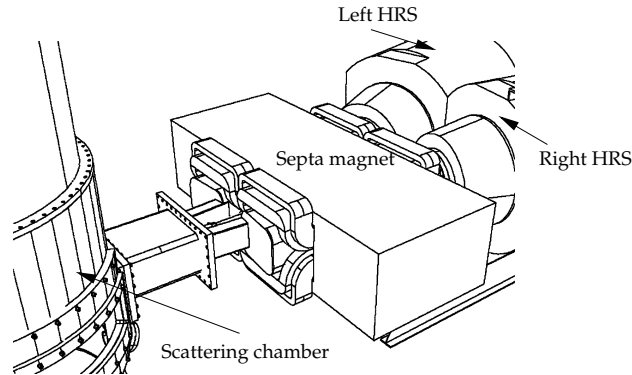


Figure 11: The drawing of the PREX setup with the septa magnet in front of the HRS spectrometers.

For PREX the nominal scattering angle is 5° and the HRS momentum is 1.05 GeV. The magnet design also allows higher-momentum operation, which is achieved by installing extra coils to boost the magnetic field. The “g2p” experiment will use the septa for central momenta of 3.3 GeV and 6° scattering angle [56]. The highest-energy configuration for APEX requires lower fields, as it calls for bending of 2.23 GeV particles to 5.5° .

The configuration of the septa magnet for e^+e^- running as required for APEX experiment will require magnetic shielding of the beam line. The TOSCA calculation of the septa field with the required iron shield was presented by P. Brindza at the “Searching for a New Gauge Boson at JLab” workshop [57].

The APEX test run confirmed that optics quality achievable with the room-temperature septum is on the level of 0.2 mrad [58]. Because the optics is calibrated via the so-called sieve slit method [58] (software spectrometer), the APEX experiment (as well as “g2p” experiment [56]) has a much less stringent field uniformity requirements than PREX, which used a hardware focus for the GHz electron flux to the integrating detector.

4.4 The detector package

The components of the two HRS detector packages are shown in Figure 12. These detector packages are designed to perform various functions in the characterization of charged particles passing through the spectrometer. These include providing a trigger to activate the DAQ electronics, collecting tracking information (position and direction), precise timing for time-of-flight measurements and coincidence determination, and identification of the scattered particles. The timing information is provided from scintillators, as well as the main trigger. The particle identification is obtained from a gas Cherenkov detector and lead-glass shower counters. A pair of VDCs provides tracking information. The main part of the detector package in the two spectrometers (trigger scintillators and VDCs) is identical; the arrangement of particle-identification detectors differs slightly. The optics of the HRS spectrometers results in a narrow distribution of particle trajectories in the transverse direction,

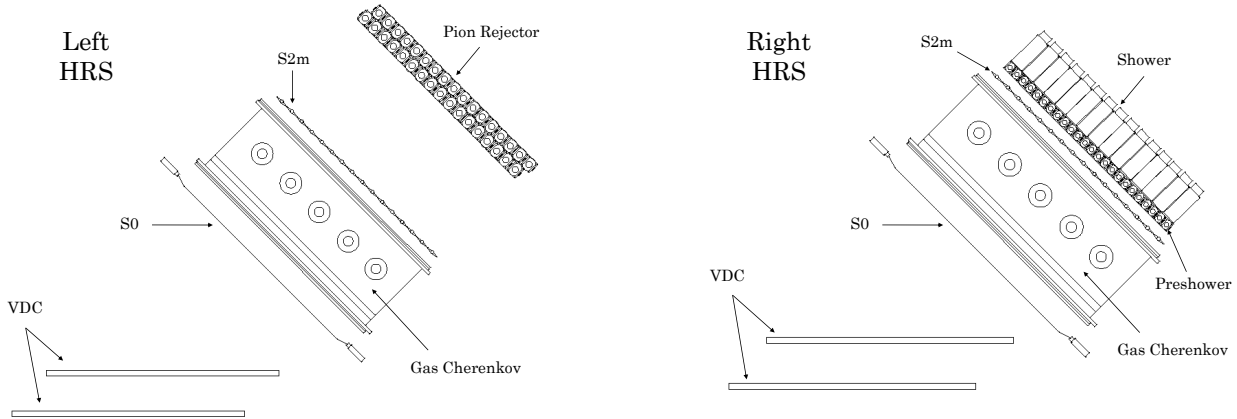


Figure 12: Sideview of detector stack for the left and right HRS. Individual elements of the detector system are indicated in the configuration used for APEX. The position of the data-acquisition (DAQ) electronics and of the VDC support frame are not shown.

leading to an aspect ratio of the beam envelope of about 20:1 at the beginning of the detector package and 4:1 at the end.

The detector package and all DAQ electronics are located inside a Shield Hut (SH) to protect the detector against radiation background. Figure 12 shows side views of the detector setup for the two HRS's.

4.5 Identification of electrons and positrons

The HRS spectrometer detector packages are equipped with gas Cherenkov counters and two-layer lead-glass calorimeters for identification of electrons and positrons. At low counting rate ($\lesssim 30$ kHz) the combined pion rejection factor (from the Gas Cherenkov and from the calorimeter) in an offline analysis is at least as high as 10,000. Particle ID is significantly degraded in the negative-polarity arm, because of the high flux of electrons.

Much lower rejection power is required for the APEX experiment, because:

- The electron to pion ratio is larger than 1/3.
- The positron to pion ratio is larger than 1/100.
- Even a pion contamination at the level of 20% in the event sample after an offline analysis is acceptable and will not adversely affect the sensitivity of the proposed experiment.
- Real $e^-\pi^+$ coincidences have a very low rate at the proposed momentum setting of the HRS, where we require both particles to carry a momentum close to half the beam energy.

The primary particle-ID consideration for APEX is the rejection of π^+ in the right HRS by incorporating the Gas Cherenkov counter in the trigger, as discussed in 4.7 and 8.9. In the test run, this was demonstrated to allow *online* pion rejection by at least a factor of 30, with some further improvements possible.

In an offline analysis, a rejection of π^+ by a factor of 100 in HRS-R is more than sufficient, and readily achieved. Indeed, in high-current tests (see section 8.4 and [59]) during the APEX test run with positron rates comparable to the expected rates for settings in this proposal, offline pion rejection of 1/48 (using the Gas Cherenkov detector alone) and 1/60 (using the calorimeters alone) were achieved, leading to a combined rejection well in excess of the desired 1/100. The expected limit to our pion rejection capability arises from e^+/π^+ coincidences in HRS-R, but this again occurs for well under a percent of pions.

4.6 Measurement of the particle track

There are two 2-m long vertical drift chambers (VDC) in the HRS detector package. These are used for the measurement of the track's coordinates and its direction in the focal plane. Each chamber has 368 wires in each “U” and “V” direction. The chamber provides coordinate resolution of at least 0.2 mm. The average number of wires per track is 4–5 depending on the track angle with respect to the chamber plane. The distance of 500 mm between the chambers allows determination of the track direction with angular resolution of 0.5 mrad. In the standard configuration chambers are instrumented with the LeCroy 2735 amplifier/discriminator cards and the LeCroy 1877 multi-hit FASTBUS TDC. The 4.0 kV HV and three component mixture (Ar-Ethane(50-50)/ethanol(0°C)) are used in Hall A VDC.

4.6.1 High-rate operation of the VDC

The VDC in the left arm needs to operate at a rate up to ~ 5 MHz (from electron singles) for one of the proposed settings. Although operation at such a high rate is not very common, the VDC's can operate at such a high rate. This was demonstrated with the test run. The preliminary analysis of the high rate VDC data from the test run demonstrates at least 60% reconstruction efficiency at 5 MHz track rate (without using hit correlations between the VDC clusters and the S2m, which should improve the efficiency further). For more information about the test run analysis results see the Section 8.10 and the report by S. Riordan at the “Searching for a New Gauge Boson at JLab” workshop [60].

The considerations below were presented to PAC35 and confirmed very well in the test run.

The operation of the HRS tracking at a total rate higher than 100 kHz is not very common. However, the track rate of 30-50 kHz of elastic scattering events from a ^{12}C target was used during many HRS optics calibrations and provides a good test case. The rate of elastic events corresponds to the track density of about 10 kHz per cm of the chamber length. The length of the focal plane and the chamber is about 2 m. This means that the resolution is not affected at the rate of 2 MHz for the whole chamber at standard operational voltage. During the recent BigBite experiment, the MWDC operated with a high detection efficiency with a hit rate of 20 MHz or 100 kHz per wire. The operation at such high rates required the development of custom-made electronics, which reduce the signal from the wire by a factor of 5. These electronics are available and were installed in the HRS for the test run – the full run would also need to make use of these electronics. Reduction of the required signal amplitude by a factor of 5 means that in each hit there will be 5 times fewer ions. The reduction of the ion cloud charge directly translates to an additional factor of 5 in rate capability, which brings the VDC limit to at least 10 MHz for the whole chamber. The

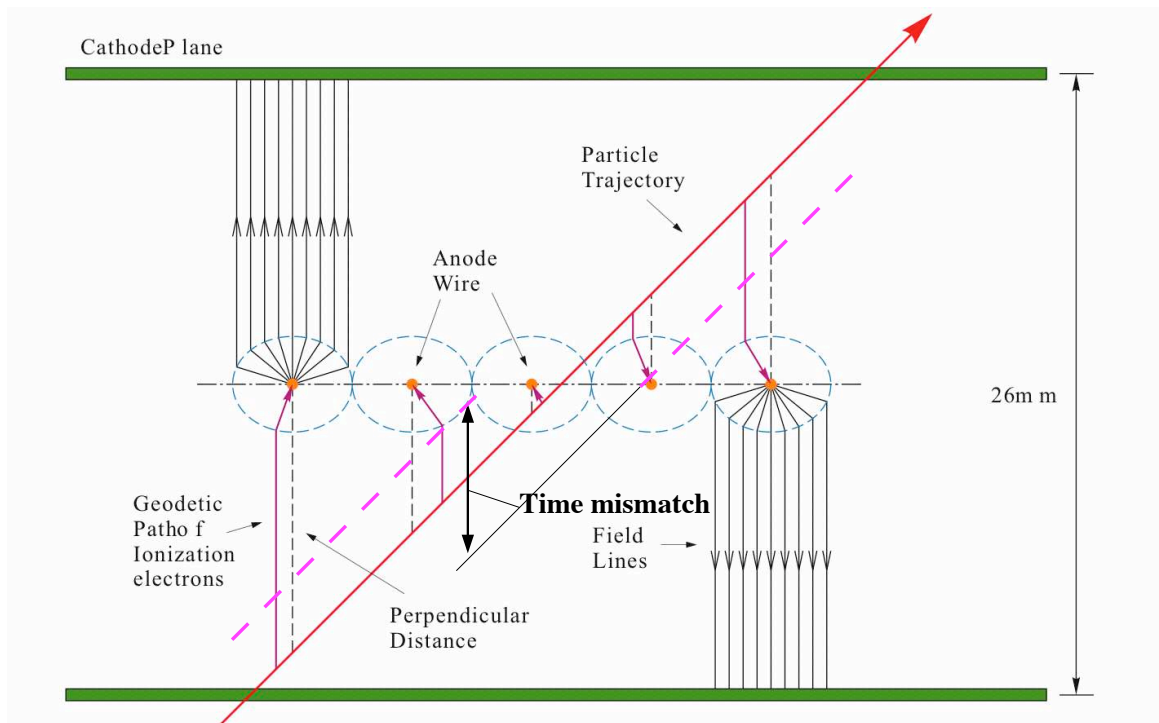


Figure 13: The illustration of the VDC drift pattern. The real track (the solid red line) has a well matched “time” between the “upper” and the “lower” times. The accidental track (the dashed violet line) has a large mismatch.

development of a new A/D card based on the MAD chip was presented in our contribution to the 2007 Hall A annual report [61].

The probability of losing a track can be estimated as follows: The VDC has a maximum drift time of 350 ns, which corresponds to 1.75 accidental tracks per event at 5 MHz. The drift time recorded for the wires of the accidental track will have a mismatch relative to the trigger time, which allows such tracks to be rejected. The rejection factor is defined by the ratio of the width of the mismatch time distribution, about 300-500 ns, to the width of the time window required for full efficiency of the real coincidence tracks, which is about 25 ns. Figure 13 illustrates the location of the track ions from the correct track and the shifted accidental “track”, the later has mismatched timing. The rejection of accidental tracks will be done for individual U and V planes before reconstruction of the X/Y coordinate. The rejection factor of 10 reduces the number of accidental tracks from 1.75 per event to 0.2 per event. Because this rejection factor is independent for two VDC chambers, the probability of an accidental track being reconstructed in both VDCs (four planes) will be at most 0.05. In these remaining 5% events, the real track will be determined using the fact that its trajectory intersects the proper scintillator paddle of the high resolution plane that is segmented into 16 paddles. As a result, the probability of a false track drops below 0.005.

For an average event, the wire multiplicity is 4.5, so the probability of having two tracks inside one group (5 wires) is less than 3%. Such events will most likely be rejected and lead to small tracking inefficiency.

4.7 Trigger and DAQ configurations

The main trigger for this experiment is given by a coincidence between signals from the two arms. The coincidence logic will use a 20 ns wide time interval for overlap between the S2m in the left and right HRS, and 40 ns wide signals of the gas Cherenkov in the left and right HRS and lead glass detectors in the left and right HRS. The expected rate of the accidental events in such triple coincidence logic is at or below 3 kHz for some of the proposed kinematics, which is well below the hard DAQ limit of 5 kHz, and with the present Hall A DAQ leads to approximately 10% dead time. We plan to use several additional triggers with wider gates prescaled by a factor of 10-100 for monitoring of the accidental events. Detailed information about the trigger and online timing achieved in the test run is given in Section 8.9. We also refer the reader to the report by E. Jensen and S. Abrahamyan at the “Searching for a New Gauge Boson at JLab” workshop [59].

4.8 HRS optics quality

The following results were obtained from elastic scattering data taken at $E_0 = 2000$ MeV on a thin ^{12}C target with the vacuum coupling between the scattering chamber and the HRS. An example of a momentum spectrum obtained with the septa magnet and 6° degree scattering angle is shown in Figure 14. The full width at half maximum is 1×10^{-4} , which is in agreement with the HRS design parameters.

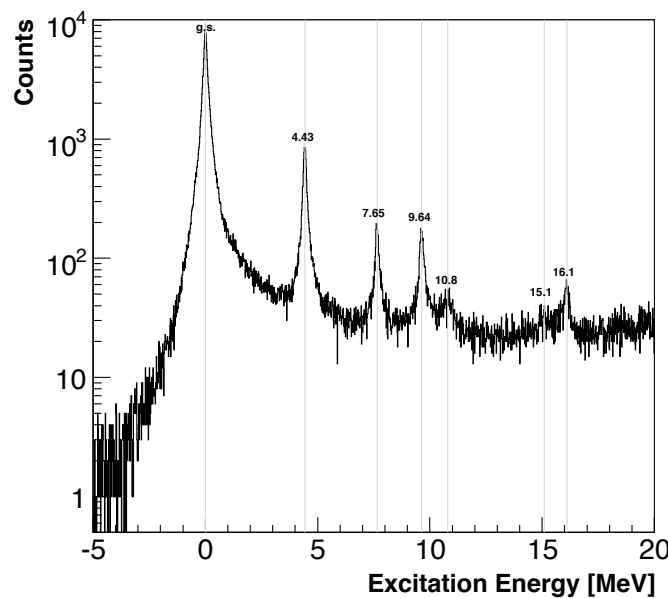


Figure 14: The momentum of the scattered electron in the $^{12}\text{C}(e, e')$ reaction, indicating a FWHM of 1×10^{-4} (relative). The beam energy was 2000 MeV, the scattering angle 6° .

The angle reconstruction parameters will be calibrated by using the well developed method of sieve slit. An example of the optics pattern is shown in Figure 15.

The accuracy of the angle reconstruction inside the spectrometer acceptance relative to the central angle has typically been done at the level of 0.2 mrad. The absolute calibration of the

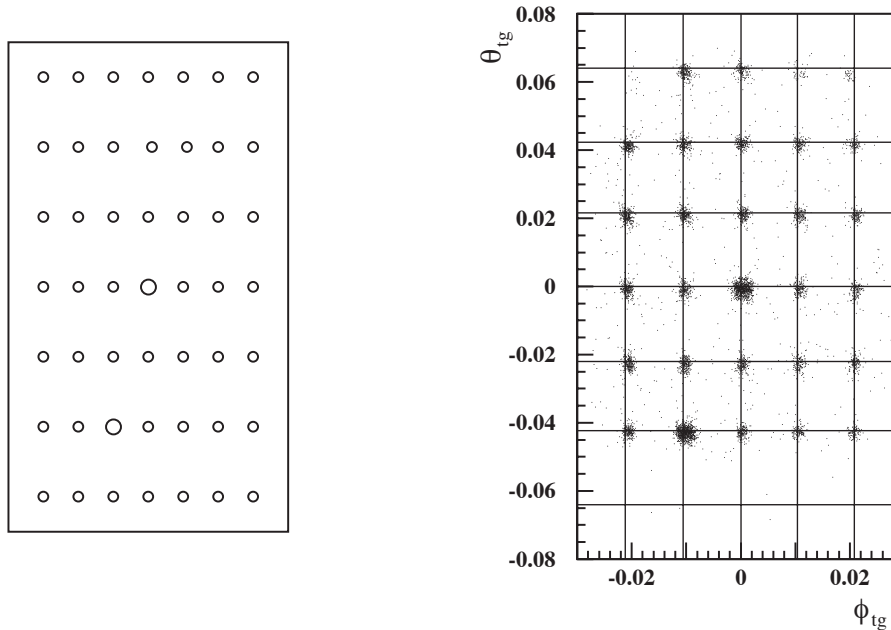


Figure 15: Geometric (left) and reconstructed (right) configurations of the sieve slit. The large holes, which allow for an unambiguous identification of the orientation of the image at the focal plane, can be clearly identified in the right figure.

central angle of the spectrometer requires an additional consideration. In this experiment the sieve slits will be mounted in front of the septum magnet, and the distance between central holes in two sieves could be measured extremely accurately. However, an uncertainty of 0.3 mm, corresponding to a central angle uncertainty of 0.5 mrad, is sufficient for this experiment as discussed in 8.3.

We discuss the optics calibration of the test run data in Section 8.

4.9 Parameters of the HRS

A complete description of the Hall A instrumentation was published in NIM-A article [55], from which we obtain the information in Table 1.

These parameters correspond to a point target and do not include the effects of multiple scattering in the target and the windows in between the scattering chamber and the spectrometer. In the calculation of the invariant mass resolution the effect of multiple scattering in the target was taken into account. In the proposed experiment, we have a vacuum coupling of the scattering chamber and the spectrometer, which means that we do not have the above-mentioned windows.

5 Signal and Trident Kinematics and Search Strategy

The stark kinematic differences between QED trident backgrounds and the A' signal are the primary considerations in determining the momentum settings of the spectrometers. As we will show in Section 6, QED tridents dominate the final event sample after offline rejection of accidentals, so we consider their properties in some detail here.

Table 1: Main design characteristics of the Hall A High Resolution Spectrometers at nominal target position. The resolution values are for the FWHM.

Configuration	QQD _n Q Vertical bend
Bending angle	45°
Optical length	23.4 m
Momentum range	0.3 - 4.0 GeV/c
Momentum acceptance	-4.5% < $\delta p/p$ < +4.5%
Momentum resolution	1×10^{-4}
Dispersion at the focus (D)	12.4 m
Radial linear magnification (M)	-2.5
D/M	5.0
Angular range HRS-L	12.5° - 150°
HRS-R	12.5° - 130°
Angular acceptance: Horizontal	± 30 mrad
Vertical	± 60 mrad
Angular resolution : Horizontal	0.5 mrad
Vertical	1.0 mrad
Solid angle at $\delta p/p = 0, y_0 = 0$	6 msr
Transverse length acceptance	± 5 cm
Transverse position resolution	1 mm

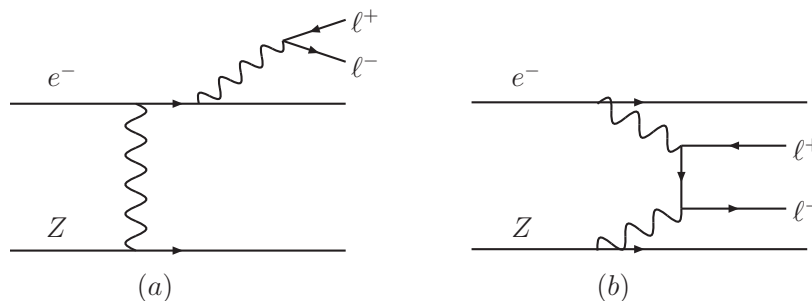


Figure 16: Sample diagrams of (a) radiative trident (γ^*) and (b) Bethe-Heitler trident reactions that comprise the primary QED background to $A' \rightarrow \ell^+ \ell^-$ search channels.

The irreducible background rates are given by the diagrams shown in Figure 16. These trident events can be usefully separated into “radiative” diagrams (Figure 16(a)), and “Bethe-Heitler” diagrams (Figure 16(b)), that are separately gauge-invariant.

We have simulated the production of these continuum trident background events in QED using the nuclear elastic and inelastic form-factors in [51]. The simulation is done using MadGraph and MadEvent [62] to compute the matrix elements for $e^- Z \rightarrow e^- (e^+ e^-) Z$ exactly (at tree-level), but neglecting the effect of nuclear excitations on the kinematics in inelastic processes. The MadEvent code was modified to properly account for the masses of the incoming nucleus and electron in the event kinematics, and the nucleus is assumed to couple with a form-factor G_2 defined in Appendix A.

The continuum trident background was simulated including the full interference effects between the diagrams in Figure 16. In addition, a “reduced-interference” approximation simplifies the analysis and is much less computationally intensive. In this approximation, we treat the recoiling e^- and the e^- from the produced pair as distinguishable. Furthermore, we separate trident processes into the radiative diagrams (Figure 16(a)) and the Bethe-Heitler diagrams (Figure 16(b)), and we calculate the cross-section for both of these diagrams separately. This approximation under-estimates the background rates by a factor of about 2–3 in the range of A' masses and beam energies considered in this proposal. For the reach analysis discussed below, we have used differential distributions computed in the “reduced-interference” approximation, then rescaled to the cross-section for the full-interference process.

The contribution from the radiative diagrams (Figure 16(a)) alone is also useful as a guide to the behavior of A' signals at various masses. Indeed, the kinematics of the A' signal events is identical to the distribution of radiative trident events restricted in an invariant mass window near the A' mass. Moreover, the rate of the A' signal is simply related to the radiative trident cross-section within the spectrometer acceptance and a mass window of width δm by [8]

$$\frac{d\sigma(e^- Z \rightarrow e^- Z(A' \rightarrow \ell^+ \ell^-))}{d\sigma(e^- Z \rightarrow e^- Z(\gamma^* \rightarrow \ell^+ \ell^-))} = \left(\frac{3\pi\epsilon^2}{2N_{\text{eff}}\alpha} \right) \left(\frac{m_{A'}}{\delta m} \right), \quad (18)$$

where N_{eff} counts the number of available decay products and is defined below equation (15). This exact analytic formula was also checked with a MC simulation of both the A' signal and the radiative tridents background restricted to a small mass window δm , and we find nearly perfect agreement. Thus, the radiative subsample can be used to analyze the signal, which simplifies the analysis considerably.

It is instructive to compare kinematic features of the radiative and Bethe-Heitler distributions, as the most sensitive experiment maximizes acceptance of radiative events and rejection of Bethe-Heitler tridents. Although the Bethe-Heitler process has a much larger total cross-sections than either the signal or the radiative trident background, it can be significantly reduced by exploiting its very different kinematics. In particular, the A' carries most of the beam energy (see discussion in Section 3), while the recoiling electron is very soft and scatters to a wide angle. In contrast, the Bethe-Heitler process is not enhanced at high pair energies. Moreover, Bethe-Heitler processes have a forward singularity that strongly favors asymmetric configurations with one energetic, forward electron or positron and the other constituent of the pair much softer.

These properties are discussed further in the Appendix of [8], and illustrated in Figure 17, which shows a scatterplot of the energy of the positron and the higher-energy electron for the signal (red crosses) and Bethe-Heitler background (black dots). The electron-positron pairs are clearly concentrated near the kinematic limit, $E(e^+) + E(e^-) \approx E_{\text{beam}}$. Background rejection is optimized in symmetric configurations with equal angles for the two spectrometers and momentum acceptance of each spectrometer close to half the beam energy (blue box).

While the signal over background (S/B) can be significantly improved with a judicious choice of kinematic cuts, the final S/B in a small resolution limited mass window is still very low, $\sim 1\%$. A resonance search or “bump-hunt” for a small signal peak over the continuous background needs to be performed, and is described in the next section. This requires an excellent mass resolution, which has an important impact on target design (see Section 4.2

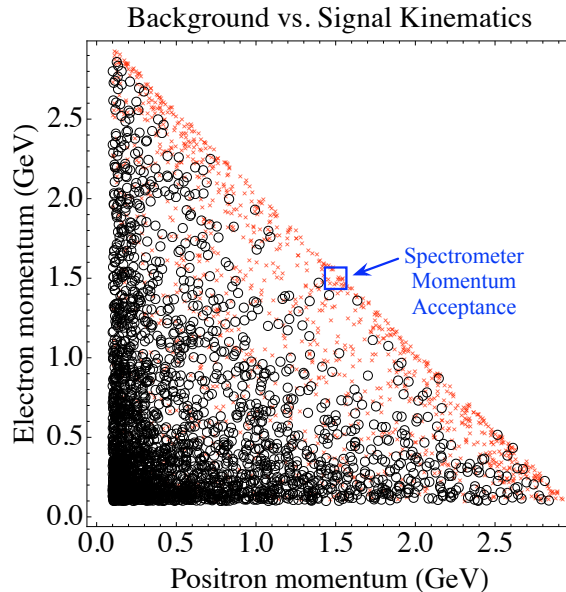


Figure 17: Positron and electron momenta in A' signal events with $m_{A'} = 200$ MeV (red crosses) and in Bethe-Heitler background events, for a 3 GeV beam energy. Comparably sized signal and Bethe-Heitler samples were used to highlight the kinematics of both; in fact the expected signals are much weaker than the Bethe-Heitler process. The clustering of A' events at high momenta near the kinematic limit and of Bethe-Heitler events along both axes are evident. A spectrometer acceptance window that optimizes signal sensitivity is indicated by the blue box.

for a discussion of the target design and Appendix B for a discussion of the mass resolution).

5.1 Statistical Analysis for Peak Search and Limit-Setting

Analysis of the APEX raw data yields an invariant mass spectrum of e^+e^- pairs. The four settings of the full APEX proposal cover a mass range from roughly 65 – 525 MeV. The low multiple-scattering in the APEX target and sieve-slit method for optics calibration allow for an excellent mass resolution $\sigma_m/m \lesssim 0.5\%$ (see Appendix B).

Here we describe the method by which we search for peaks in the spectrum, and quantify both the significance of any observed peak and the exclusion power of the experiment.

In this section, we will use as an illustrative example a “practice distribution”, obtained from the APEX test run. The test run probed a narrower mass range than the full experiment, namely from $\sim 170 - 250$ MeV, and also had ~ 100 times lower statistics than the full run at a given energy setting. Moreover, the “practice distribution” was produced using *uncalibrated optics* so that any physical peak would be smeared to a width of ~ 20 MeV — therefore the examples shown here can only be taken as estimates of the test-run’s eventual sensitivity.

5.1.1 Searching for a Resonance: a rough preliminary outline

We will formulate the significance of a resonance as the probability of the accidental appearance of the observed signal.

A rough outline of the procedure to look for a resonance is as follows. We scan along the spectrum, and at each mass bin we hypothesize a Gaussian peak of an unknown height and width σ equal to the experimental mass resolution. For a fixed A' mass $m_{A'}$, and given hypotheses for the number of signal events S and number of background events B , we model events as distributed according to a probability distribution

$$P(m_{e^+e^-}) = \frac{1}{S+B} (S \cdot N(m_{e^+e^-} | m_{A'}, \sigma) + B \cdot \text{Polynomial}(m_{e^+e^-}, a_i)) \quad (19)$$

where $m_{e^+e^-}$ is the invariant mass of the electron-positron pair, N is a normal/Gaussian probability distribution, and the background shape is given by a polynomial with coefficients a_i . From the likelihood function, L , based on this probability model, we form a test statistic, $-2 \ln \lambda(S)$, where $\lambda(S)$ is the profile likelihood ratio,

$$\lambda(S) = \frac{L(S, \hat{B}, \hat{a}_i)}{L(\hat{S}, \hat{B}, \hat{a}_i)}, \quad (20)$$

and where $\hat{(\)}$ indicates the unconditional (conditional) maximum likelihood estimator for that parameter, arrived at via fits of the model to the data. The systematic uncertainty in the background shape is incorporated into the profile likelihood ratio via the nuisance parameters a_i , the coefficients of the polynomial. We then determine a confidence interval in number of signal events S , i.e., we determine the range in S consistent with the data at a given confidence level. The upper limit of this confidence interval corresponds to a limit on S (the conversion from a limit on S to a limit on the physical parameter α'/α is discussed in 5.1.2).

A confidence interval that does not contain $S = 0$ indicates a significant peak. However, because the search involves testing the background-only (null) hypothesis multiple times over a wide mass range, the probability of observing a large background fluctuation at *some* mass is increased. We account for this phenomenon, often referred to as the “look elsewhere effect”, by degrading the significance of any observed peak, i.e., by scaling the p-value at zero for each mass hypothesis by a “trials factor”

$$\text{p-value} \rightarrow \text{p-value} \times \frac{\text{mass range}}{\text{mass resolution}} \quad (21)$$

or equivalently in terms of the confidence level. Equivalently, we can insist on a smaller threshold for the (uncorrected) p-value to claim evidence of new physics.

This method is illustrated in Figure 18. The left panel shows the mass distribution for the “practice example” described above, obtained from 2% of the APEX test run data using un-calibrated optics. As such, any physical peaks in this spectrum would be smeared to a $\mathcal{O}(20 \text{ MeV})$. Nevertheless, this spectrum is useful to test our peak search method, and we perform a scan using a purposely unrealistic mass resolution of $\sigma = 2 \text{ MeV}$ to show the rough sensitivity of the test run data. Note that, by design, no physical peak could possibly be observed in this scan. (Moreover, this scan assumes worse mass resolution than is expected in the final analysis, and may therefore underestimate the final sensitivity of the test run data.) The right plot in Figure 18 shows the uncorrected p-value for the background-only hypothesis and the 2σ threshold before and after correcting for the look elsewhere effect.

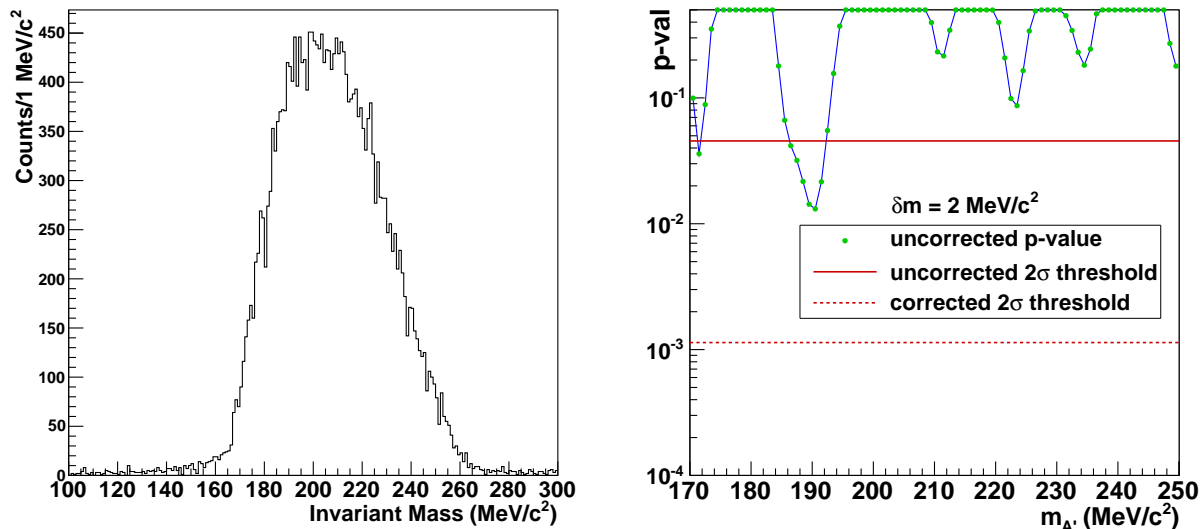


Figure 18: Example of searching for a significant peak caused by an A' . **Left:** A practice example mass spectrum of 2% of the APEX test run data, with no optics analysis (the resulting mass resolution is much worse than it is after a full optics analysis). **Right:** The p-value (not corrected for the look-elsewhere effect) for the background-only hypothesis for each hypothesized mass $m_{A'}$, calculated as a result of a scan of the “practice distribution,” assuming a purposefully unrealistic mass resolution of $\delta m = 2 \text{ MeV}/c^2$. Note the change in range of the x -axis. Also shown are the 2σ threshold before (solid horizontal line) and after (dashed horizontal line) correcting for the look-elsewhere effect. The upper limit on the p-value range is 0.5, corresponding to a significance of zero. For the entire mass range, $S = 0$ has a p-value above the corrected 2σ threshold (dashed line) therefore no significant peaks are observed.

Because the p-value does not drop below the dotted line, we conclude (as expected) that no significant peak is observed in this practice scan.

In the event that a significant resonance is found, there are several cross-checks that can be performed to convince oneself that the resonance is from an A' . Since the A' cross-section scales in a known way as a function of angle, beam energy, and target thickness, it is also known how the number of signal events change as a function of these variables. It is thus relatively easy to convince oneself that a real peak has been found.

5.1.2 Setting Limits on α'/α

The process of setting limits on the A' cross section does not need to account for the look elsewhere effect; for a given mass spectrum, we translate the (uncorrected) 2σ upper limit on the raw signal rate S into an upper limit on α'/α using a modified form of Eq. (18),

$$\epsilon^2(m_{A'}) = \frac{S_{\delta m}}{B_{\delta m}} \frac{F(m_{A'})}{m_{A'}} \frac{\delta m}{\left(\frac{2N_{\text{eff}}\alpha}{3\pi}\right)}, \tag{22}$$

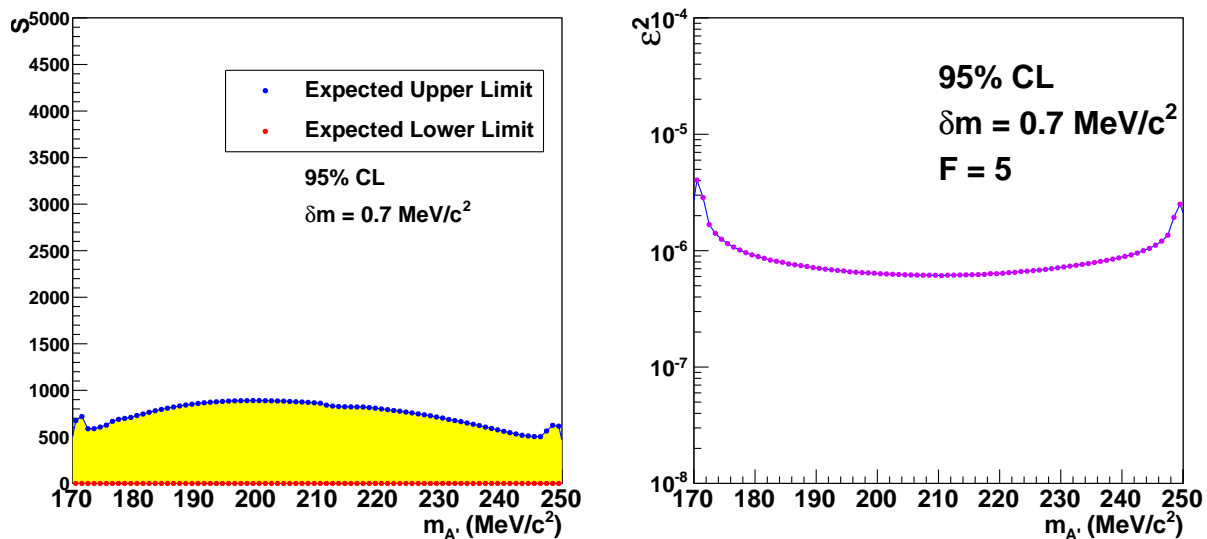


Figure 19: Left: Upper and lower limits on the number of signal events S at the 95% CL. Right: Projected sensitivity for 2σ limit on $\epsilon^2 = \alpha'/\alpha$ for the APEX test run.

where $S_{\delta m}$ ($B_{\delta m}$) indicates the number of signal (background) events within a mass window determined by the mass resolution, δm , and where F is a scaling factor arising from the normalization of the total trident background to the radiative sub-process (Figure 16(a)),

$$F = \frac{\text{No. trident events}}{\text{No. Radiative trident events}}. \quad (23)$$

Preliminary estimates based on limited Monte Carlo samples indicate that F has weak mass dependence over the range of the test run, and that $F \approx 5$; that value is used here.

To obtain a preliminary estimate as to the expected reach in α'/α of the test run, we fit a polynomial to the mass spectrum of the 2% of test run data with no optics analysis, mentioned in the previous section. We then use this polynomial to generate pseudodata sets with statistics equal to that of the test run data, i.e., 1.44 million events. Applying our limit setting procedure then yields the upper and lower limits on S and the resulting projected expected upper limits on $\epsilon^2 = \alpha'/\alpha$ for the test run, presented in Figure 19.

5.2 Smoothness of the invariant mass acceptance

The experiment will search for a narrow peak in the invariant mass spectrum of e^+e^- pairs, whose resolution should be as high as possible and at least much better than the width of the acceptance. Because a high level of statistical precision is needed, it is especially important to have a very small level of systematics in the proposed experiment. The systematics arise from variations in the acceptance and detection efficiency.

The pair invariant mass is $m_{\pm}^2 \approx 2m_e^2 + p_+ \cdot p_- \cdot [(\theta_+ + \theta_-)^2 - \theta_+ \theta_- \phi^2]$, where p_+ , p_- are the positron and the electron momenta, the θ_+ , θ_- are the scattering angles, and the ϕ is an angle between the scattering planes. The efficiency for a given value of m_{\pm} is defined by an integral over all the phase space of the detector system. The most important part of this integral is over p_+ , p_- , θ_+ , and θ_- . The range of the momentum for one of the particles in the pair (p_+ or p_-) each leads to about 10% variation in m_{\pm}^2 . The range for the scattering angles (θ_+ or θ_-) each leads to about 25% variation of m_{\pm}^2 . Thus, for example a 10% dip in spectrometer efficiency for a narrow window of positron momenta ($dp \sim 1\%$) would, when integrated over the other variables, give rise to a broad dip, spread over the full range of masses and with local magnitude reduced by a factor of $10 \times (25)^2 = 6250$, so the 10% dip becomes a 0.0016% step, which is even smaller than the size of statistical fluctuations in the proposed sample of $10^7 - 10^8$ events. Moreover, even a larger correction of this broad shape would be absorbed into the polynomial parametrization of the smooth background, not interpreted as a signal.

Monte Carlo studies have been done to evaluate the effect of such irregularities. For example, to study the effect of irregularities in angular acceptance we have excluded a window of $2 \text{ mrad} \times 2 \text{ mrad}$ in the positron spectrometer only, and for the momentum acceptance, we excluded within a window of 1130 to 1135 MeV/c, again for the positron spectrometer only. We then formed an invariant mass spectrum and performed our scan.

For mass resolutions of $\delta m = 0.5, 0.7,$ and $1 \text{ MeV}/c^2$, irregularities in the momentum or angular acceptances do not result in significant peaks in the invariant mass spectrum. Example spectra, one for a full spectrum after excluding events in the momentum acceptance and the other for the excluded events, are shown in Figure 20.

5.3 Calculation of the ϵ reach

For all cross sections and rates of reactions described in this proposal, Monte Carlo based calculations were performed over a grid of beam energy settings and central spectrometer angular settings. Interpolation was used to extend this grid continuously to intermediate beam energies and angles — all rates exhibited expected power law behavior, thereby providing confidence in the reliability of an interpolation. Additional cross checks at specific points were performed to test the accuracy of our interpolation, which was generally better than $\sim 5\%$.

In order to calculate the α'/α reach of the proposed experiment for a particular choice of target nucleus, spectrometer angular setting, and momentum bite, the following procedure is performed:

- Monte Carlo events are simulated for the Bethe-Heitler, radiative tridents, and the continuum trident background including the full interference effects between the diagrams. The latter background is computationally intensive, and only a small statistics sample is generated, sufficient to obtain the cross-section from MadEvent.
- The cross-section ratio of the full continuum background (with interference effects) to the sum of the Bethe-Heitler and radiative tridents is calculated, and represents a multiplicative factor by which the latter must be multiplied to get the background cross-section.

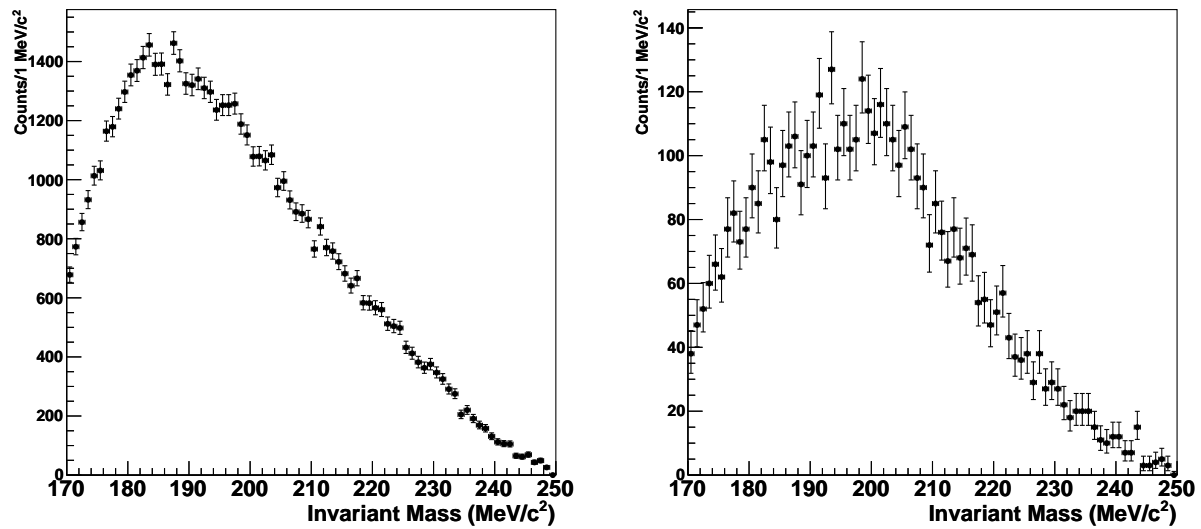


Figure 20: Investigating irregularities in the acceptance. Left: Invariant mass spectrum of e^+e^- pairs from ~ 70000 simulated Bethe-Heitler and radiative trident background events, where events with a positron with momentum from 1130 to 1135 MeV/c in the positron spectrometer have been excluded. Right: The events excluded as a result of creating an irregularity in the momentum acceptance. The excluded events are distributed smoothly across the mass range, and hence no significant peaks result. The events excluded due to an irregularity in the angular acceptance (not shown) are similarly distributed.

- The rates of all reactions impinging the spectrometer acceptance were calculated by integrating over a chosen target profile, which usually extended from 4.5 to 5.5 degrees. For Bethe-Heitler, radiative tridents, and the continuum trident background, the calculation of the rate was performed as a function of invariant mass.
- Using the expressions in Appendix B, we calculated the mass resolution δ_m . We then tiled the acceptance region with bins of size $2.5 \times \delta_m$ in invariant mass.
- As a function of α'/α , the total number of signal (S) and background (B) events was calculated with the help of the formulas in Section 3 for each bin.
- We then set $S/\sqrt{B} = 2$, and solved for α'/α .

This procedure was used to calculate the reach in the α'/α and $m_{A'}$ parameter space shown in Section 7.

6 Backgrounds

In this section, we present an analysis of the backgrounds in the data. Table 2 summarizes the expected singles rates, trigger rates, and coincidence rates (including both true coincidences and those accidentals that cannot be rejected in an offline analysis). The remainder of this section elaborates on these rates, and related physics considerations.

We present calculations of the electron, pion, and positron singles rates in Section 6.1. These rates were checked against measurements made by experiment E03-012 for a 5 GeV electron beam incident on a hydrogen target, with at 6° 2-GeV HRS setting. They were also checked with the data obtained during the APEX test run. The pion rates were obtained by means of the “Wiser” code [63], with corrections described in Section 6.1.2 based on the results of the APEX test run; positron singles rates from trident reactions were calculated using MadGraph and MadEvent [62], described in Section 5. The considerations of Section 6.2 determine trigger rates and upper bound on offline accidental rates shown in Table 2.

Besides the trident events discussed in Section 5, an additional source of true coincidence events is the “two-step” (incoherent) trident process, in which an electron radiates a real, hard photon in the target that subsequently converts to a high-mass e^+e^- pair. We discuss a calculation of this rate in Section 6.3. For thin targets, it is suppressed compared to the trident rate, and so it is sub-dominant for all the settings we consider.

6.1 Inclusive rates

There are three main contributions to the counting rate in the spectrometers at small angles. They are due to electrons, pions, and protons scattered into the HRS acceptance. We discuss electron, pion, and proton singles rates below. The positron singles rates are dominated by trident events in which only the positron enters the spectrometer acceptance. These rates have been calculated for each spectrometer setting using the same techniques as for pair production, discussed in Section 5.

Settings	A	B	C	D
Beam energy (GeV)	2.2	4.4	1.1	3.3
Central angle	5.0°	5.0°	5.0°	5.0°
Effective angles	4.5–5.5	4.5–5.5	4.5–5.5	4.5–5.5
Target T/X_0 (ratio ^a)	4%	8%	0.7% (1:3)	8%
Beam current (μA)	70	60	50	80
Central momentum (GeV)	1.095	2.189	0.545	1.634
Singles (negative polarity)				
e^- (MHz)	4.1	0.7	4.5	2.2
π^- (MHz)	0.1	1.7	0.025	0.9
Singles (positive polarity)				
e^+ (kHz)	27	5	18	17
π^+ [p] (kHz)	90	1700	25	900
Trigger/DAQ:				
Trigger ^b (kHz)	3.0	3.1	2.0	3.3
Coincidence Backgrounds:				
Trident: $e^-Z \rightarrow e^-e^+e^-Z$ (Hz)	500	110	260	370
e^+e^- from real γ conversion (Hz)	30	16	3	45
Accidentals ^c (Hz)	55	30	40	40

^a For settings A, B, and D the target is taken to provide uniform coverage of the theta range from 4.5 to 5.5 degrees. For setting C (1-pass), the target is taken to be concentrated at the ends of the angular acceptance, so that the effective angles are 4.5 and 5.5 degrees, with three times more material at the downstream end (5.5 degrees) than the upstream end (4.5 degrees).

^b Trigger: Coincidence in 20 ns time window, assuming π^+ rejection by a factor of 30 by including GC in trigger.

^c Dominated by e^+e^- accidental rate, but π^\pm contributions are also included. We assume offline π^+ rejection by a factor of 10^2 , π^- rejection by a factor of 3, a 2 ns time window and additional factor of 4 rejection of accidentals from the target vertex (all of these rejection factors are quite conservative). Further rejection using kinematics is expected, but not included in the table.

Table 2: Expected counting rates for proposed experiment. Settings A and B comprise the primary run plan, while settings C and D are additional possible settings at intermediate energies that may be possible in early running.

6.1.1 The electron singles rates in HRS

The three contributions to the electron rate in the HRS at the proposed momentum settings are:

- Inelastic scattering
- Radiative elastic electron-nuclei scattering
- Radiative quasi-elastic electron-nucleon scattering.

The differential cross section of inelastic eN scattering processes is written in the standard notation as

$$\frac{d^2\sigma}{dE'd\Omega_{e'}} = \frac{\alpha^2}{4E^2 \sin^4\left(\frac{\theta}{2}\right)} \left[W_2(q^2, \nu) \cos^2\left(\frac{\theta}{2}\right) + 2W_1(q^2, \nu) \sin^2\left(\frac{\theta}{2}\right) \right]. \quad (24)$$

For $E, E' \gg M_N$ and finite q^2, ν , we will use

$$\frac{d^2\sigma}{dE'd\Omega_{e'}} \approx \frac{\alpha^2}{4E^2 \sin^4\left(\frac{\theta}{2}\right)} \frac{F_2(q^2, \nu)}{\nu}. \quad (25)$$

For the elastic (quasi-elastic) process with low momentum transfer and very small scattering angle only the contribution from Coulomb scattering is important. The radiative elastic scattering cross section can be estimated as

$$\begin{aligned} \frac{d^2\sigma}{dE'd\Omega_{e'}} \approx & \frac{\alpha^2}{4(E')^2 \sin^4\left(\frac{\theta}{2}\right)} \times \\ & \{ Z^2 \cdot F^2(E'\theta) \times \left[\left(\frac{\alpha}{\pi} \ln\left(\frac{E'\theta}{m_e}\right)^2 + t_{eff} \right) / (E - E') \right] \times \left[1 + \left(\frac{E'}{E}\right)^2 \cdot F^2(E\theta) / F^2(E'\theta) \right] + \right. \\ & \left. Z \times \left[\left(\frac{\alpha}{\pi} \ln\left(\frac{E'\theta}{m_e}\right)^2 + t_{eff} \right) / (E - E') \right] \times \left[1 + \left(\frac{E'}{E}\right)^2 \right] \right\}, \end{aligned}$$

where $F(E'\theta)$ is the nuclei elastic form factor at three-momentum transfer equals to $E'\theta$ and t_{eff} is the effective target thickness in units of radiation length. The effective target thickness t_{eff} has two parts. The first one is a probability of an internal radiation before scattering $\frac{\alpha}{\pi} \ln(E'\theta/m_e)^2$. The second accounts for the probability of an external radiation before scattering, which is about half of the target thickness. The form factor of the tungsten nucleus for very low values of q can be estimated from its radius $R \approx 7$ fm as $(1 - (qR)^2/6)$ and for sufficiently high q from a Fourier transform of the density approximated by a step function. The radiation after scattering taken is taken into account by the term proportional to $(\frac{E'}{E})^2$.

6.1.2 The pion singles rates in the HRS

The differential cross section for the electro-production of pions can be written as

$$\frac{d^3\sigma}{dE'd\Omega_{e'}d\Omega_{\pi}} = \Gamma \cdot \frac{d\sigma_{\gamma^*,\pi}}{d\Omega_{\pi}}, \quad (26)$$

where Γ is the virtual photon flux factor given by

$$\Gamma = \frac{\alpha}{2\pi^2} \frac{E'}{E} \frac{s - M^2}{2MQ^2} \frac{1}{1 - \epsilon}, \quad (27)$$

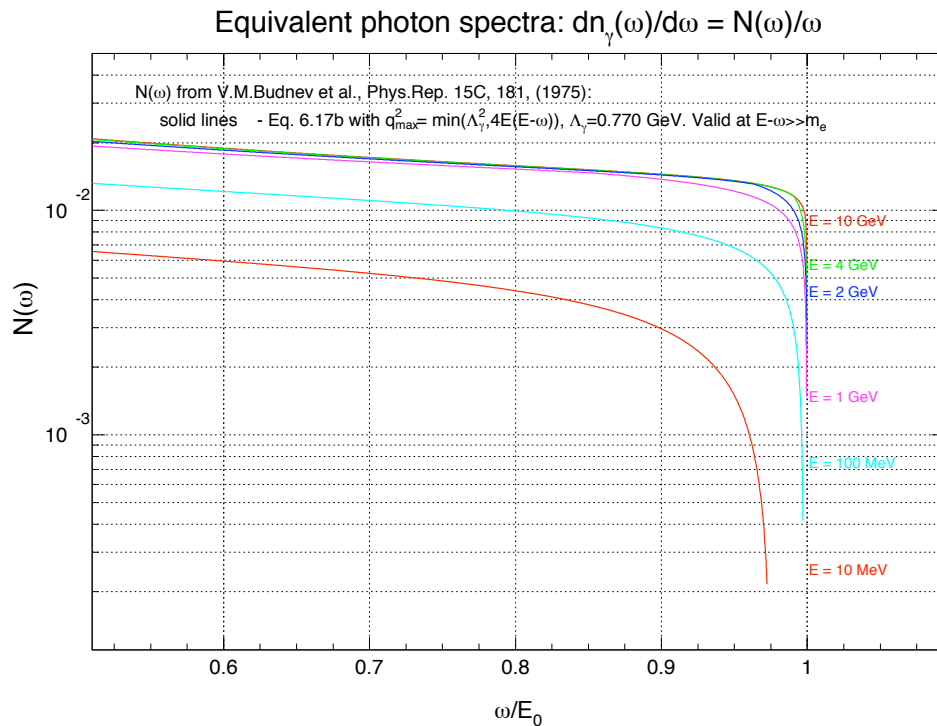


Figure 21: The photon flux factor according to the effective photon approximation [64].

and $\frac{d\sigma_{\gamma^*,\pi}}{d\Omega_\pi}$ is the cross section for pion production by the virtual photon. Integration over the electron scattering angle leads to an estimate of $\Gamma \approx 0.015$, see Figure 21. At small scattering angles, where $Q^2 \ll \nu^2$, only transverse terms of the cross section contribute. Our calculations of the cross-section were performed using the “EPC” code [65] with a normalization factor of 1.5 obtained from our measurements of a 5 GeV electron beam on a hydrogen target with the HRSs at 6° and 2 GeV/ c settings [66]. At these kinematics, the prediction of the Wiser code [63] is in very good agreement with our experimental data.

The Wiser code is based on a fit to pion yields in electron-scattering experiments with beam energies of 5 GeV and higher. Therefore, we expect that the extrapolation to lower beam energies may be unreliable. We have found that the ratio of π^+ to e^+ singles observed during the test run (2-pass beam) is significantly lower than the Wiser prediction, by roughly a factor of seven. The pion rates for setting “A” in Table 2 have been adjusted to include this correction. We expect that the pion rates for setting “D” (3-pass) will also be lower than the Wiser calculation, but by a smaller factor; though the rate is therefore somewhat uncertain, we have assumed a factor of 2.5 reduction relative to Wiser.

It should be noted that this uncertainty has very mild impact on the final sensitivity estimates in the proposal. For example, if the pion rates in the table are a factor of 2 larger

Table 1
 $E d^3\sigma/d^3p$ [$\mu\text{b}/\text{GeV}^2$] at $E_\gamma = 3.2$ GeV, $\theta_{\text{lab}} = 2^\circ$

x_π	π^+	π^-	x_p	p	x_K	K^+
0.994	15.1 ± 0.41	—	0.854	2.94 ± 0.23	—	—
0.900	32.3 ± 0.76	49.7 ± 1.0	0.746	4.75 ± 0.34	0.977	4.05 ± 0.23
0.838	48.9 ± 1.4	77.5 ± 1.8	0.673	6.81 ± 0.58	0.902	4.49 ± 0.52
0.806	54.5 ± 1.5	67.2 ± 1.6	0.635	8.10 ± 0.54	0.865	3.35 ± 0.47
0.775	61.6 ± 1.9	56.4 ± 2.7	0.598	9.26 ± 0.70	0.827	4.07 ± 0.62
0.712	72.9 ± 2.6	57.7 ± 2.9	0.521	13.0 ± 1.1	0.751	3.05 ± 0.64
0.618	85.2 ± 5.0	64.0 ± 4.9	0.400	24.6 ± 2.6	—	—
0.524	76.9 ± 6.90	73.5 ± 5.7	0.272	33.7 ± 4.4	—	—
0.429	90.9 ± 9.53	68.7 ± 8.5	0.132	54.3 ± 7.2	—	—
0.381	84.3 ± 9.94	92.0 ± 8.6	0.056	54.7 ± 8.7	—	—
0.333	102.0 ± 11.60	80.0 ± 10.0	0.026	61.9 ± 12.8	—	—

Figure 22: The hadron production cross section from [67].

than expectations, the coincidence trigger rate can be brought down to 3 kHz by reducing the beam current by roughly $2^{1/2}$, which affects the α'/α sensitivity by a factor of $2^{1/4} \approx 1.19$, leading to a $\sim 15\%$ reduction in sensitivity.

6.1.3 The proton singles rates in HRS

There were several measurements of the inclusive hadron yield in the reaction $H(\gamma, h)X$ at energies of several GeV, see e.g. [67, 68, 69]. In addition, there is a recent measurement of the electro-production by a 5 GeV beam [66]. There are three computer codes, which allow us to calculate the hadron production cross section: the so-called Wisner code [63], the EPC code [65], and the DINREG event generator in GEANT [70].

The overall result is that the proton yield at the proposed kinematics will be about 4 to 6 times lower than the pion yield, as illustrated in the table in Figure 22. Here the Feynman variable is $x = p_{\parallel,cm}^h/p_{max,cm}^h$. For example, for $E_{beam} = 3.2$ GeV, $\theta = 5^\circ$ the particle momentum 1.6 GeV/ c corresponds to the $x_\pi = 0.50$ and the $x_p = 0.48$. The resulting yield ratio of protons to pions is $1.0/5.5$ before correcting for the pion decay, or $1.0/4.2$ at the focal plane.

6.2 True and accidental coincidences

The accidental coincidences between the electron and the positron arms will be a dominant part of the recorded events. A typical composition of the single rate in the spectrometers (for 2-pass running) is expected to be $e^-/\pi^- \approx 41/1$ in the negative polarity arm and $\pi^+/e^+ \approx 3.3/1$ in the positive polarity arm. An example of the relative time distribution between the signals of two arms in Figure 23. Selection of the true coincidence events, which are mostly $e^-\pi^+$, within a 2 ns time window allows us to calibrate the detector timing offsets, using production data, and optimize the tracking analysis.

The true coincidence e^+e^- events will be selected by:

- The 2-ns coincidence time window;

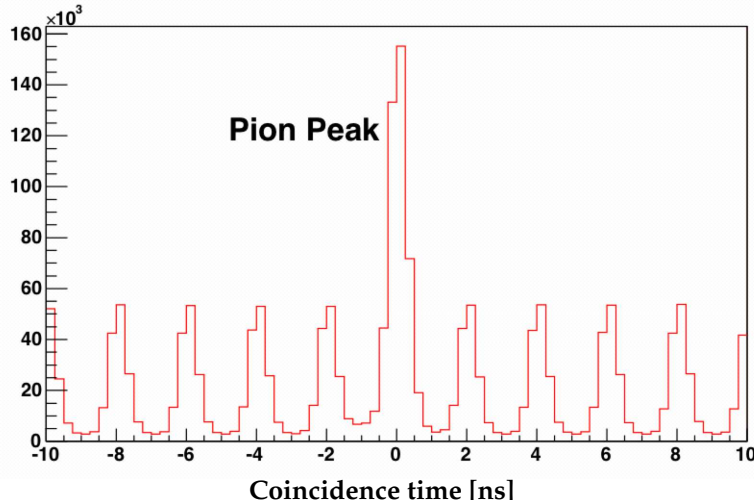


Figure 23: The event distribution over relative time between signals of two arms.

- The 5-cm target vertex correlation between arms;
- Gas Cherenkov & shower calorimeter identification in both arms.

With this selection, the irreducible background of trident events (electroproduction of e^+e^- pair dues to QED) is expected to dominate the background (from accidental e^+e^- and true $e^-\pi^+$ events) at least by order 5 – 10 to 1 for all settings, so that this contamination should not affect sensitivity for the search of the narrow resonance.

6.3 Electron-Positron Pairs from Conversion of Real Photons

We have already discussed the principal source of electron-positron pairs, namely the trident process, in Section 5. An additional reaction that gives rise to high-energy electron-positron pairs is the “two-step” (or incoherent) trident process, consisting of radiation of a hard photon in the front of the target, followed by the conversion of this photon to a high-mass pair further along the target. The rate for this process evidently goes as T^2 , and it can be $\mathcal{O}(1)$ for $T \sim 0.1$.

At a point t radiation lengths into the target, the intensity of photons carrying a fraction $x = E/E_0$ of the beam energy is approximately [71]

$$I_\gamma(t, x) \approx \frac{1}{x} \frac{(1-x)^{4t/3} - e^{-7t/9}}{\frac{7}{9} + 43 \log(1-x)}. \quad (28)$$

The photoproduction process was then simulated to determine the pair rate within spectrometer acceptance, in the case of photons carrying the entire beam energy ($x = 1$). For spectrometer windows centered near $p = E_0/2$, the spectrometer acceptance grows linearly from $x_{min} = 2p_{min}/E_0$ to $x = 1$, and vanishes below x_{min} . In this approximation, we have integrated (28) over x and over the thickness of the target to obtain the numbers in Table 2. Even for the thickest targets considered, two-step trident events represent only a 30% correction to the total e^+e^- pair rate. We have also computed the contribution of two-step tridents to the positron singles rate, which is negligible.

7 Proposed measurements

We propose a twelve-day run in the configuration “B” of Table 3 (see also Table 2) and six-day runs in each of the remaining configurations, to search for new resonances in e^+e^- trident spectra from 65 to 525 MeV. Settings “A” and “B” are the primary run plan, using nominal beam energies for 12 GeV running. The settings “C” and “D” correspond to additional configurations that may be allowed in early running and would expand the range of the experiment’s sensitivity. For settings “A” and “C”, the target thickness and beam current have been optimized to accumulate the largest possible sample of trident events without saturating the data acquisition system. Settings “B” and “D” are far from data acquisition limits, but we do not use $T/X_0 > 10\%$ to avoid limits on the total radiation produced.

The mass range from 65 to 525 MeV is chosen to take advantage of the Hall A HRS spectrometers, as well as for its theoretical interest. Lower masses are more effectively probed by vertexing experiments. Settings at higher masses are possible but have significantly reduced sensitivity and are better suited to exploration with higher-acceptance equipment and an experiment optimized to accept muon and pion pairs as well as electrons.

As illustrated in Figure 24, the sensitivity of the experiment is greatly enhanced by including the intermediate-energy settings “C” and “D”. At beam energy E , a spectrometer setting with opening angle θ and momentum acceptance near $E/2$ is sensitive to A' masses $\approx \theta E$. Each spectrometer setting is sensitive to A' resonances 15% higher or lower than the optimal mass, for fixed central angle. This range is extended to $\pm 30\%$ in mass, shown in Figure 24, by using a long target. The mass range from 120 to 550 MeV could be covered (with reduced sensitivity) using only the 2.2 and 4.4 GeV beam energy settings, but using multiple nominal central angles.

In each setting, the proposed experiment will accumulate between 70 and 300 million trident events. With these statistics, it will be possible to search offline for small resonances comprising a few thousandths of the collected data in a resolution-limited window. This will allow sensitivity to new gauge boson couplings α'/α as low as 10^{-7} over the broad mass range of the experiment, as summarized in Figure 24. This sensitivity would improve on the cross-section limits from past experiments by a factor of $\sim 100 - 1000$.

Settings	A	B	C	D
Beam energy (GeV)	2.2	4.4	1.1	3.3
Beam current (μA)	70	60	50	80
Nominal central angle	5.0°	5.0°	5.0°	5.0°
Time Requested (hrs)				
Energy change	–	4	4	4
Magnet setup	4	4	4	4
Optics calibration	16	16	16	16
10% \mathcal{L}	2	2	2	2
Normal \mathcal{L}	144	288	144	144
Total	166	314	170	170

Table 3: Run plan for the proposed experiment. Settings A and B comprise the primary run plan, while C and D are possible additional settings if flexible beam energies are permitted in early running.

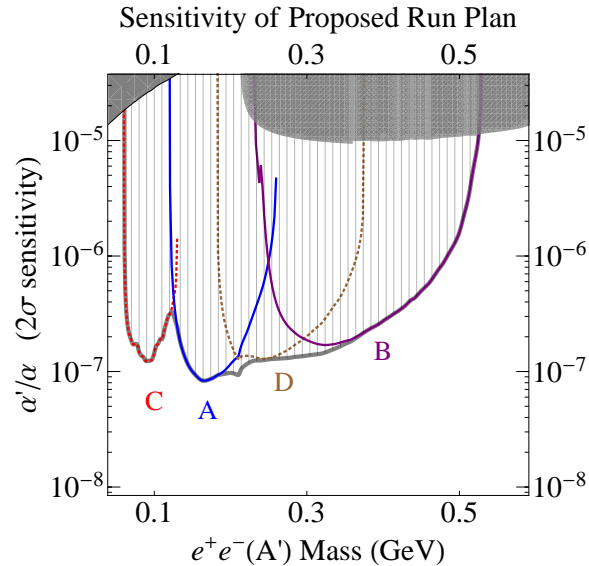


Figure 24: Expected 2σ exclusion sensitivity for ϵ for the run plan outlined in Table 3. Settings A and B comprise the primary run plan, while C and D are possible additional settings if flexible beam energies are permitted in early running, which considerably increase the range of masses over which the proposed experiment is sensitive. Existing constraints are shown in the gray shaded regions. The colored curves correspond to the sensitivity in each of the individual energy settings, and the thick gray curve reflects the sensitivity of a combined analysis. 3.

As a specific example, we have illustrated the expected sensitivity of setting A to A' signals with different ϵ in Figure 25. Each component of the target populates a different invariant mass distribution; for simplicity we consider only the contribution from the front planes of the target, with $\theta_{eff} \approx 5.5^\circ$. The left panel illustrates the absolute size of A' signals at $m_{A'} = 200$ MeV compared to the continuum trident background (gray line) and the size of 2 and 5-sigma statistical fluctuations (blue and green dashed lines), while the right panel illustrates how the same signals would appear after subtracting a smooth parameterization of the background. The purple curves in each panel corresponds to an A' signal with $\alpha'/\alpha = 7 \cdot 10^{-6}$ at 200 MeV, which according to the estimates in Section 2.4 would not be seen or excluded at 2σ by a future KLOE search in $\phi \rightarrow \eta A'$. The red curve has $\alpha'/\alpha = 1.3 \times 10^{-7}$, corresponding to the expected “ 5σ ” sensitivity (not accounting for the trials factor) in the proposed experiment.

7.1 Beam time request

The beam time request for the proposed experiment is summarized in Table 4.

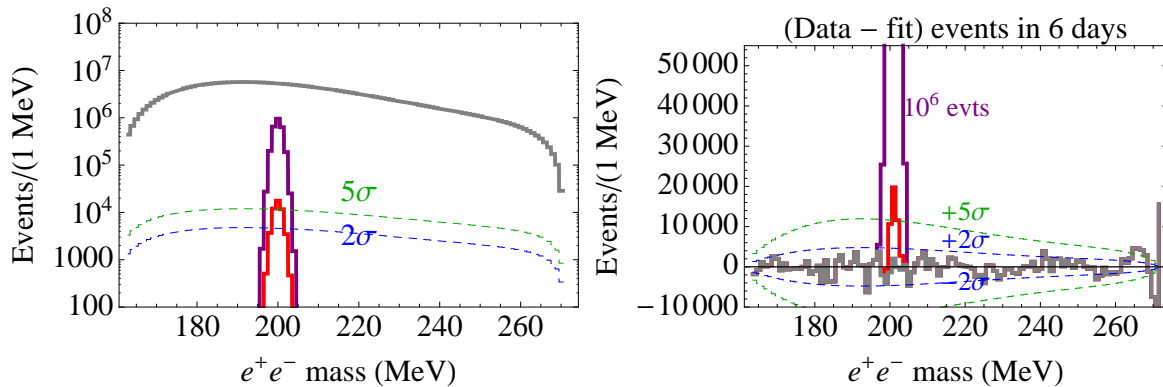


Figure 25: Comparison of signal rates in six days of running at setting A to expected background and statistical sensitivity. **Left Figure:** The resonances in purple and red lines correspond to A' signals at 200 MeV, smeared by a Gaussian to model detector resolution and multiple scattering, with $\alpha'/\alpha = 6.5 \times 10^{-6}$ and 1.3×10^{-7} , respectively. The upper (purple) signal is just beyond the 2σ expected sensitivity of a KLOE analysis, while the lower (red) signal corresponds to the “ 5σ ” sensitivity (not including a trials factor) of this experiment. The gray line is the simulated invariant mass distribution for the continuum trident background, and the blue and green dashed lines reflect the size of 2 and 5σ Poisson fluctuations. **Right Figure:** The gray line corresponds to the bin-by-bin differences between pseudodata containing no signal and a smooth fit to this pseudodata. Analogous subtractions when a signal is present are shown in purple and red, with the same ϵ as in the left figure. Again the blue and green dashed lines reflect the size of 2 and 5σ Poisson fluctuations.

Settings	A	B	C	D
Beam energy (GeV)	2.2	4.4	1.1	3.3
Beam current (μA)	70	60	50	80
Target thickness (X_0)	4%	8%	0.7%	8%
Beam on target (hrs)	162	306	162	162
Time Requested (hrs)	166	314	170	170
	\rightarrow 820 (\sim 34 days total)			

Table 4: Beam time request for the proposed experiment. Settings A and B comprise the primary run plan, while C and D are possible additional settings if flexible beam energies are permitted in early running. Including these settings would increase by a factor of two the mass range of maximal sensitivity, as illustrated by the curves in Fig. 24.

8 The concerns identified by PAC35

The proposal was submitted and presented to PAC35, which granted its conditional approval. The PAC35 report on the proposal PR12-10-009 is shown on the next page. In additional communication, the reviewer in PAC35 recommended a test run in order to do the following (we show in brackets the subsection in which we address the concern):

1. Run with the zig-zag mesh design of the tungsten target and prove that it allows the requested vertex resolution (see Section 8.2).
2. Prove that it is possible to reach the uncertainty of 0.1 mrad in determining the central scattering angle between the two spectrometers (see Section 8.3).
3. Prove that it is possible to use the gas Cherenkov counters in the trigger to help clean pions. In fact the TAC report claims that this is not possible with total rates/PMT at the level of a few hundred Hz to MHz. Also prove that the off-line rejection of 10,000:1 can be achieved (see Section 8.4, Section 8.5, and Section 8.6).
4. Detailed description of different contributions to background and their importance (how assumptions and/or approximations can influence the predictions) and comparison with measurement (see Section 8.7).
5. Prove that a 20 ns (S0-S0) and 40 ns (S0-S0-C) can be achieved (see Section 8.8 and Section 8.9).
6. Prove that the vertical drift chambers (VDCs) can operate at a rate higher than 20 kHz/wire (that, according to the TAC report, is the maximum Hall A has operated until now) (see Section 8.10).
7. If it is possible (not obvious for a test run) it will be advisable to set the septum magnets at higher fields to prove that also at energies higher than 2 GeV it is possible to reach the uniformity of the field requested from the experiment (see Section 8.11).

In the following we present the results of our investigation of the issues raised in the PAC35 report and the results of the test run in June 2010 (see also the reports at the “Searching for a New Gauge Boson at JLab” workshop [72]). We summarize our response to the PAC 35 concerns in Section 8.12.

8.1 The PAC35 report

Individual Proposal Report

Proposal: PR12-10-009

Scientific Rating:

Title: Search for new Vector Boson A' Decaying to e^+e^-

Spokespersons: R. Essig, P. Schuster, N. Toro, B. Wojtsekhowski

Motivation:

The proposal is to search for a vector boson A' with weak coupling to electrons in the mass region 65-550 MeV. The proposed search is motivated by recent developments of models trying to explain inconsistencies observed in astrophysical data and dark matter search experiments. Such a vector boson would couple to charged leptons as it will mix with photon. If A' is produced by radiation off an electron beam, it would decay producing very narrow resonance in the invariant mass e^+e^- spectrum.

The proposal is very interesting and has the potential to make an important discovery. There are not many places where such measurement can be done, as it requires very high integrated luminosity and good control of the electromagnetic background. Part of the plane of coupling constant *versus* mass of the boson has already been excluded, but the region available for the proposed experiment coincides with the domain of greatest theoretical interest, for example explaining the deviation from SM expectations observed in the latest $g-2$ experiment.

Measurement and Feasibility:

The experiment is proposed to run in Hall A. It will measure the invariant mass spectrum of electron-positron pairs produced by scattering an electron beam with 75 μ A on a long (50 cm) tilted high-Z Tungsten wire mesh target. The electron and positron will be detected in coincidence in the HRS magnetic spectrometers. For the mass range of interest, the spectrometer will be positioned at small angles (5°), which can be achieved using the recently constructed septum magnet. The proposed run plan is for the 12 GeV running period, using 4 energy settings at 1.1, 2.2, 3.3 and 4.4 GeV and 2 angle settings for a total of 33 days beam time.

Issues:

The measurements proposed cover a very interesting range with a large potential for discovery which can change the picture of interactions and our understanding of physics beyond the Standard Model. Even if a signal is not seen, the experiment will constrain the plane of new boson mass and coupling allowed and so provide important limits on the domain of possible new physics.

However, running conditions push the detector performances to the extreme in terms of relative angular resolution (positioning of spectrometers), acquisition rate, particle identification. The feasibility of the measurements relies on a detailed understanding of the experimental conditions as well as on the proper background estimates.

Taking into account the very high requirements on the detectors and strong dependence of the obtained results on the understanding of very high background, the PAC recommends tests of as many elements of the proposed setup as possible as well as detailed study of the calculated background and comparison with measurements. *The PAC strongly encourages the collaboration to continue the development of the proposal.*

Recommendation: Conditional approval

The experiment requires careful preparation and detailed commissioning studies before it can run. Without these, the results might not attain the credibility they deserve.

8.2 The multi-foil target (reviewer’s comment 1)

A special multi-foil target was constructed for the test run, although it was never installed due to time constraints. The multi-foil target presents a superior design over the wire-mesh target originally described in the PAC 35 proposal and mentioned in the reviewer’s comment 1. We describe the new target in detail in Section 4.

We note that the observed vertex resolution in the Pentaquark experiment is 1.1 cm (see [73]). This is more than sufficient to resolve foils separated by 5 cm. Moreover, to achieve the conservative rejection of accidentals assumed in Table 2, it suffices to resolve tracks coming from foils separated by more than 10 cm.

8.3 The relative angular resolution (reviewer’s comment 2)

Here we address the reviewer’s comment 2, regarding the “**relative angular resolution (positioning of spectrometers)**”.

The high sensitivity of the proposed experiment to a potential A' -boson signal relies on both high statistics and fine resolution of the e^+e^- pair invariant mass.

The latter is dominated by the accuracy of determination of the relative horizontal angle between the e^+ and e^- trajectories. This in turn has three components. The first is multiple scattering in the target, which in our proposal is significantly reduced by using a multiple-foil target (see Section 4), and is on the level of $0.4/p[\text{GeV}]$ mrad in each arm (for spectrometer central momentum p), contributing 0.5 MeV to the pair invariant mass resolution for A' decays within the target foil. The second contribution is due to the HRS detector resolution (including the magnification effects of magnetic optics). The third contribution is due to the imperfect reconstruction of target coordinates from focal plane coordinates — during the test run, several measurements were performed indicating that angular calibration at the level of 0.2 mrad (more details can be found in the report by J. Huang at the workshop “Searching for a New Gauge Boson at JLab” [58]). The second and the third contributions combined lead to an uncertainty of roughly 0.5 mrad in each arm (which is consistent with previous calculations [55]), and contributes $0.7 \text{ MeV} \cdot p [\text{GeV}]$ to the pair invariant mass resolution.

Other kinematic resolutions contribute much less to the pair invariant mass resolution. Due to the very large dispersion in the HRS, particle momenta are measured to within a few $\times 10^{-4}$, which contributes negligibly to the pair invariant mass resolution (e.g. a fractional momentum resolution 5×10^{-4} contributes a mere $0.07 \text{ MeV} \cdot p [\text{GeV}]$ to the pair invariant mass resolution). The 1 mrad uncertainty in the vertical angles is also relatively unimportant, contributing just $0.12 \text{ MeV} \cdot p [\text{GeV}]$ to the pair mass resolution.

Spectrometer positioning accuracy The difference between the two HRS central angles, i.e. the precise **positioning of the spectrometers** defines the absolute scale of the pair invariant mass, but contributes only at higher order to the event-by-event mass resolution. For example a 1 mrad error in this angle would shift the reconstructed mass scale by about 0.5%, but contribute a mere 8×10^{-5} to the event-by-event invariant mass resolution.

The angle between the spectrometers can be determined by measuring the distance between the central holes in the two sieve slits and the distance between the sieve slit plane and the center of the target. The distance between the central holes in the sieve slit of the two HRSs, 140 mm, was measured to the relative accuracy of 0.002 (which corresponds to

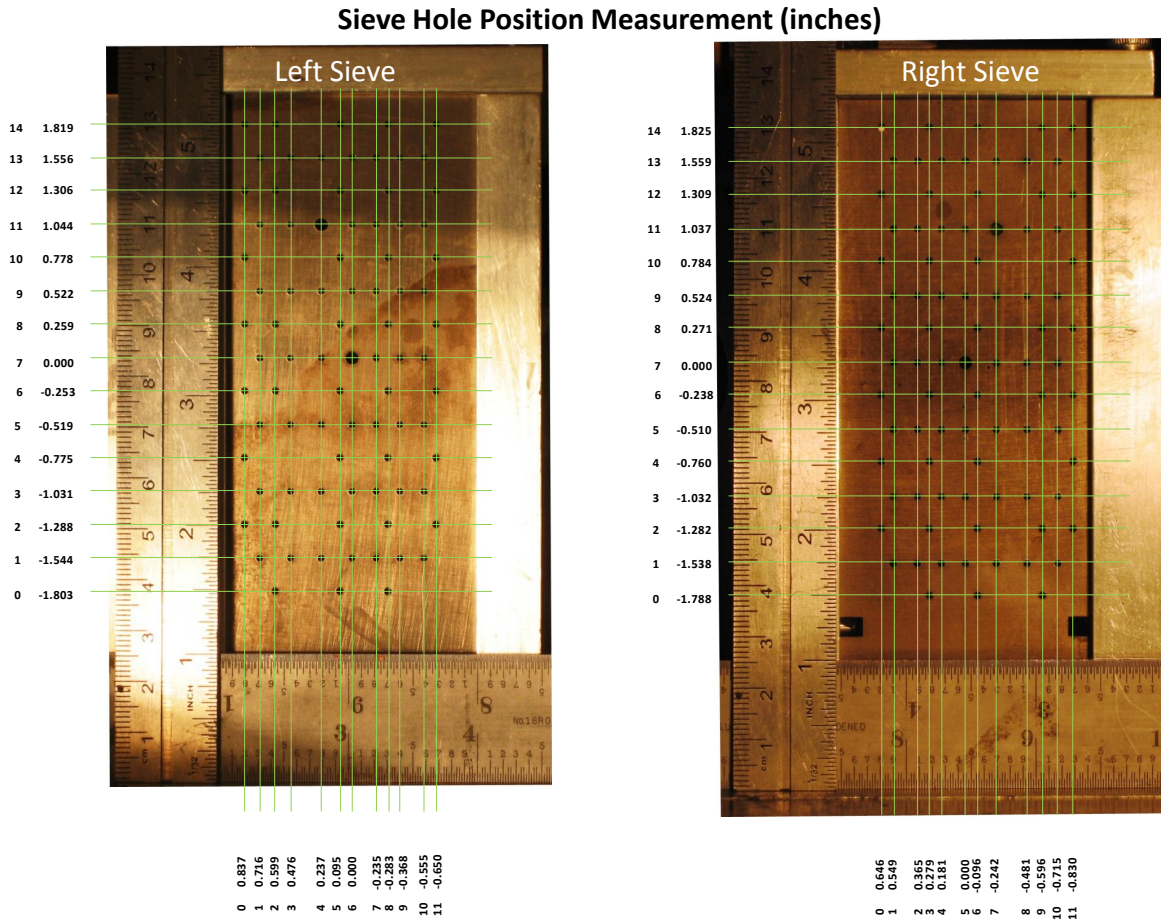


Figure 26: The picture of the sieve slit with the ruler on the bottom used to measure the distance between the central holes of the two sieve slits.

the 0.3 mrad angle) with just a simple ruler and a camera, as is shown in Fig. 26. A similar approach will be used to measure the distance between the target and sieve.

8.4 Particle identification (reviewer’s comment 3)

Here we address the issue of “particle identification” (reviewer’s comment 3).

The advantageous feature of this experiment is that the particles of interest are the electrons and the positrons. There are two types of detectors in the HRSs for particle identification. They are the gas Cherenkov counter (GC) and the two-layer lead-glass calorimeter (LG). The GC is sensitive to high energy electrons and positrons and sufficiently blind to pions (and muons) in the momentum range of interest for this experiment. Specifically, the probability of a pion’s inducing any signal in the GC is less than 2%, and the rejection factor at least on the order of 50. The LG detectors in both HRSs have good segmentation and amplitude resolution, which allows a pion rejection factor of at least 100 and limited by same-arm accidental coincidences with electrons or positrons. Performance of the particle ID in the APEX test run is summarized in Sections 8.5 and 8.6.

Each of the PID detectors of the HRS could be used in the trigger. The simplest trigger

setup, used in many HRS experiments and described in this proposal, uses only the GC in the right HRS. This trigger was used in the APEX test run and demonstrated to reject pions by a factor of at least 30. Such a rejection factor is sufficient for the reduction of the DAQ rate. An additional online pion rejection could be obtained with a slightly more elaborate trigger. In particular, greater π^+ rejection could potentially be achieved by using the LG calorimeter in the coincidence trigger as well. The necessary electronics for the total sum from the LG calorimeter has been implemented but not used. Likewise, online rejection of pions in the left HRS could be implemented. Pion rejection in the left HRS is more difficult than in the right HRS because of the high e^- singles rate and the resulting significant probability of accidental signals (we expect that a factor of 10 rejection could still be achieved even at 2.5 MHz e^- rate). However, the electron/pion ratio in the left HRS is 1/3 or higher, so pion rejection in the left HRS is not crucial.

We stress that these additional pion rejection approaches are not necessary nor have they been assumed in this proposal; they would however allow for somewhat higher-current operation and therefore higher statistics by roughly 30%.

In an offline analysis, high segmentation of the LG, in combination with superior timing resolution of S2m, provides the best approach for PID, and will add a factor of more than 10 to the overall pion rejection factor.

We discuss the PID further in Section 8.5 and Section 8.6.

8.5 The lead glass calorimeter PID at high event rate (reviewer's comment 3)

Here we further address the “PID” concern (reviewer's comment 3), in particular how the lead glass calorimeter will help with PID.

The lead glass calorimeters in both arms have very good segmentation which allows operation at a rate even higher than that projected in the proposed experiment. In fact, high rate performance of the lead glass calorimeter is limited by existing DAQ, which is using 1000 ns delay lines and a 120 ns gate at ADC. However, even with such electronics we achieved sufficient results in off-line analysis, limited only by accidentals due to the wide gate at ADC. Fig. 27 shows the correlation between signals from the two layers of the calorimeter in the positron arm.

The PID in the electron arm is less demanding than that in the positron arm because the expected ratio pion/electron is less than 3. We estimated that a pion rejection factor of 3 will be sufficient in the electron arm and easily achievable by a combination of the Gas Cherenkov and Calorimeter. The electron arm lead glass calorimeter performance is illustrated in Fig. 28 for the track rate of 0.35 MHz and of 4.6 MHz (mostly electrons). It is easy to see from the right plot that the electron “ridge” has become wider due to the significant probability of the tail from the previous electron event in the ADC gate. The electron arm PID could be a bit of a concern only in kinematics D where the rate of pion is high and rate of electrons is also high. However, even in that case the pion rejection factor of 10 is expected to be achievable.

8.6 The gas Cherenkov PID at high event rate (reviewer's comment 3)

Here we further address the “PID” concern (reviewer's comment 3), in particular how the gas Cherenkov counter will help with PID.

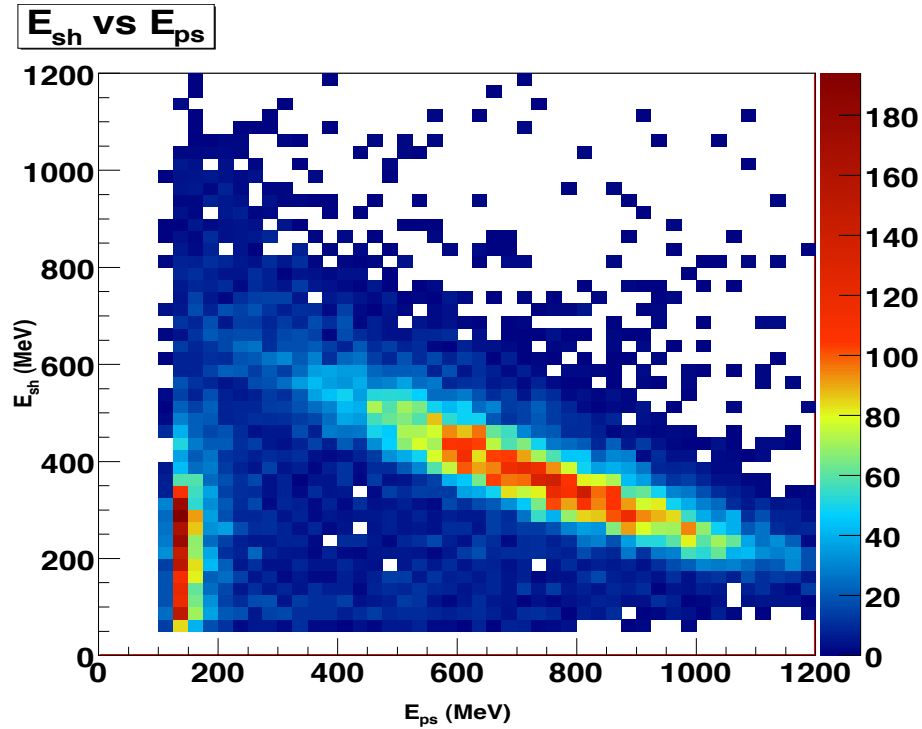


Figure 27: The PID with the lead glass calorimeter of the positron arm. Data collected at the track rate of 0.75 MHz. The scale in both E_{sh} and E_{ps} is given in MeV/channel.

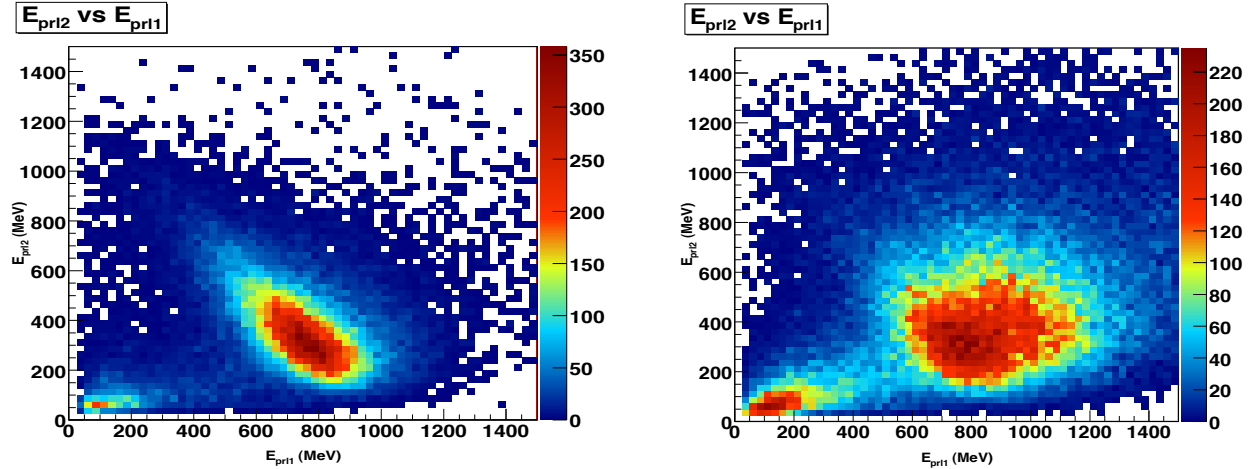


Figure 28: The PID with the lead glass calorimeter of the electron arm. Data collected at the track rate of 0.35 MHz on the left plot and 4.6 MHz on the right plot.

The detection probability of the pion in the gas Cherenkov of the HRS spectrometer is on the level of 1%, as it was measured many times, see e.g. [55]. This is why in our proposal PR12-10-009 we suggested using the GC of the positron arm in the trigger. It would allow us to reduce the DAQ rate dominated by accidental coincidence events by 20-30 times. Offline analysis of the GC information allows additional pion rejection. The amplitude distribution of the total sum (all PMT signals of the positron arm GC) is shown in Fig. 29. The pion

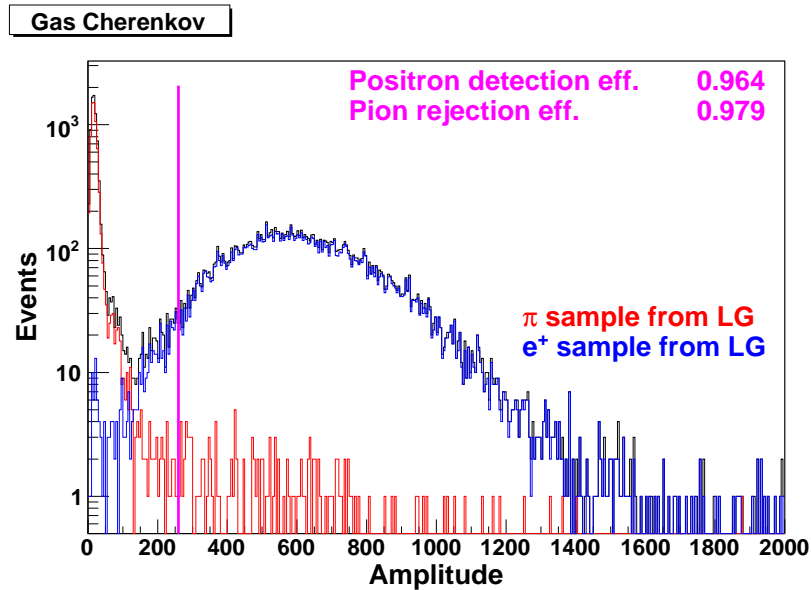


Figure 29: The PID with the gas Cherenkov counter in the positron arm at the track rate of 0.75 MHz. The off-line pion rejection factor is 48.

rejection factor is 48 for the rate at the maximum luminosity in the test run.

8.7 Backgrounds (reviewer’s comments 4)

Here we address the concern over the **“different contributions to background and their importance”** (reviewer’s comment 4).

The search for a small signal always requires evaluation of the background. The primary feature of the proposed search method is the small width of the bump. The main physics background in this experiment is due to the QED process of e^+e^- pair electroproduction through bremsstrahlung of virtual photons. This process produces a smooth mass distribution, yet its level is not reducible but defined by the ratio of coupling constants, α'/α . The second process, which also has a QED origin, is photo-production of an electron and positron pair by real and quasi real photons from the target nuclei. Any additional background, physics or accidental, leads to a relatively small loss in the experiment’s sensitivity so long as it contributes a fraction of the QED processes’ rates. This consideration allows us to find a level of acceptable non-QED background and calculate rates of such backgrounds and estimate their impact on the expected results. In addition to analyzing the smooth background, we also showed that a sudden sharp variation of the angular or momentum acceptance and the resulting size of fake bumps is negligible (see Section 5.2).

8.7.1 Test Run results

During the test run we were able to collect data off a Tantalum target used by the PREX experiment. The thickness of the target is unfortunately unknown, so we are not able to compare absolute measured rates with our calculations. We are, however, able to compare ratios of rates. We checked that, as expected, the π^\pm background rate is less than predicted with the Wisler code (see Section 6.1.2), since the beam energy is lower. We also checked that the ratio of e^+e^- coincidence pairs to e^+ singles is consistent with expectations. A detailed comparison between the test run data and the calculated rates is still work in progress.

8.7.2 Background rate

In the proposal we calculated the particle rate for several background sources: a single arm electron, a single arm positron, the e^+e^- pair production from the π^0 decay, the $\pi^+\pi^-$ pair production from the vector meson decay, and the accidental backgrounds of e^+e^- , $e^+\pi^-$, and $\pi^+\pi^-$. The most important processes are presented in Section 6.

The single arm background rate in the electron arm was calculated from the known cross section of the elastic and quasi-elastic electron scattering in which we took into account the effects of the target thickness and bremsstrahlung. We calculated the pion production rate using the Wisler code. The prediction using the Wisler code was expected to overestimate the rates at low beam energy. However, it is known with good accuracy (at least 20%) for beam energies above 5 GeV. The test run data confirmed that the pion rate is low enough to handle it by the existing PID detectors. Background is less than the Wisler code predicted, by roughly a factor of 6 for configuration ‘‘B’’ (2-pass beam energy). At intermediate energies (3-pass, i.e. configuration ‘‘D’’) we have assumed that the Wisler code over-estimates pion yield by a more modest factor of 2.5.

The e^+e^- event rate The test run results on the e^+e^- event rate confirmed our estimate that the pair yield from the π^0 decay is negligible (as expected).

An important comment We emphasize that even if we underestimated the background rates by an $\mathcal{O}(1)$ amount, we can easily lower the current to a level that the equipment can handle. The resulting loss in statistics of e^+e^- pairs will only lead to a square-root loss in sensitivity in α'/α . We would still cover a large and important part of parameter space, vastly improving over the existing constraints.

8.8 Acquisition and trigger rate (reviewer’s comment 5)

Here we address the concern about the ‘‘trigger’’.

The proposal asked for a relatively short coincidence time window of 20 ns. The test run confirmed that it is possible to use such a time window (Fig. 30). The test run shows that even a 15 ns time window could be used. A short coincidence time window helps to keep the DAQ rate sufficiently low. The offline analysis will use a 2 ns time interval for further suppression of accidental events. An offline time window of 2 ns was demonstrated in many experiments with the HRS detector.

The performance of the existing HRS data acquisition system could be characterized by the relative dead time as a function of the trigger rate and the event size. The proper use of

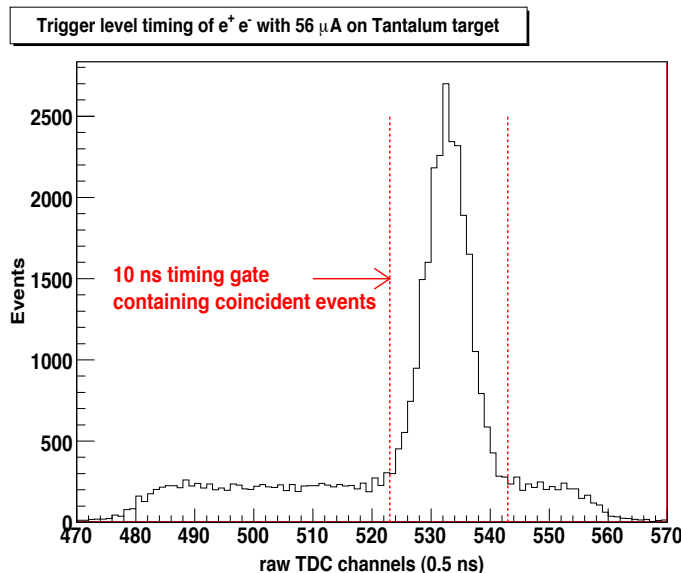


Figure 30: The event distribution versus time between the electron-arm S2m signal and the DAQ trigger signal (the DAQ trigger signal is a coincidence between the electron-arm S2m and positron-arm S2m and the positron-arm GC). The total width of the accidental coincidences is 40 ns. The real coincidence has a width of 10 ns, which is the width of the bottom part of the peak.

particle ID and the short coincidence time window in the trigger logic allow us to keep the DAQ rate sufficiently low and avoid significant loss of useful statistics. During the test run in high intensity beam operation, which corresponded to a 5 MHz track rate in the VDC on the Left arm, the Left HRS detector contributed an extra 500 bytes per event. We expect to take data with dead time on the level of 10% for a projected 3 kHz DAQ rate. This loss was taken into account in the calculation of the projected sensitivity of this experiment.

8.9 The short coincidence time window (reviewer’s comment 5)

Here we further address the “[trigger](#)” concern (reviewer’s comment 5).

The trigger was organized using coincidence between trigger scintillator planes of two spectrometers (S0/S2m) and the Gas Cherenkov counter (GC) of the positron arm, as it was proposed in PR12-10-009. We used the S2m plane, comprised of 16 counters, during high rate operation and an S0 counter at low rate. The average times for the signal from the individual PMT of S2m and GC were aligned using the S0 signal as a reference and a set of short cables, see resulting distribution in Fig. 31. Such fine tuning allowed us to implement a 40 ns coincidence time window and demonstrated that even 15 ns could be used without data losses.

8.10 The high rate operation of the VDC (reviewer’s comment 6)

Here we address the “[high rate operation of the VDC](#)” (reviewer’s comment 6).

As presented in PR12-10-009, the VDC operation at the required rate of 5 MHz for 300 wires per plane and 5 wires/plane per track is within the known range of the drift chamber regime for a 150 mm length of the sensitive section of the wire [74]. However,

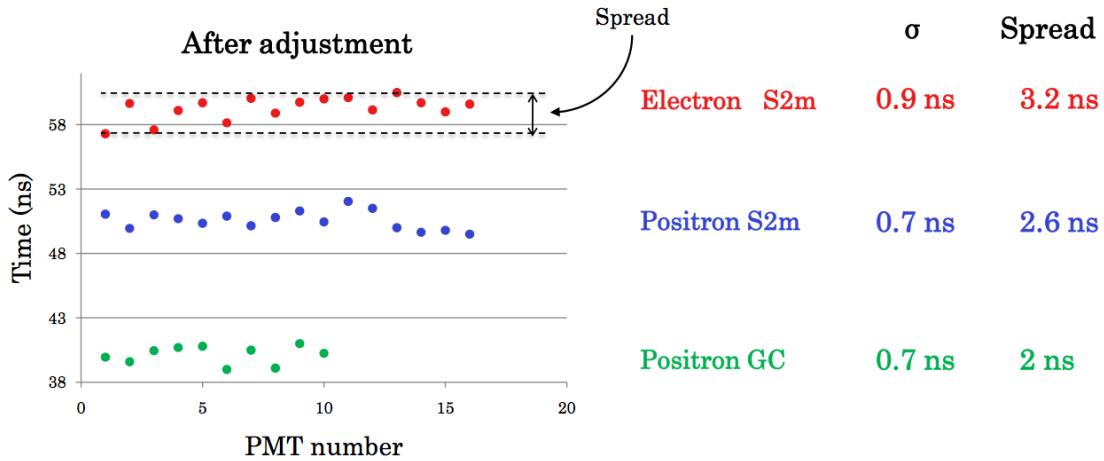


Figure 31: The alignment of the PMTs average time in trigger detectors.

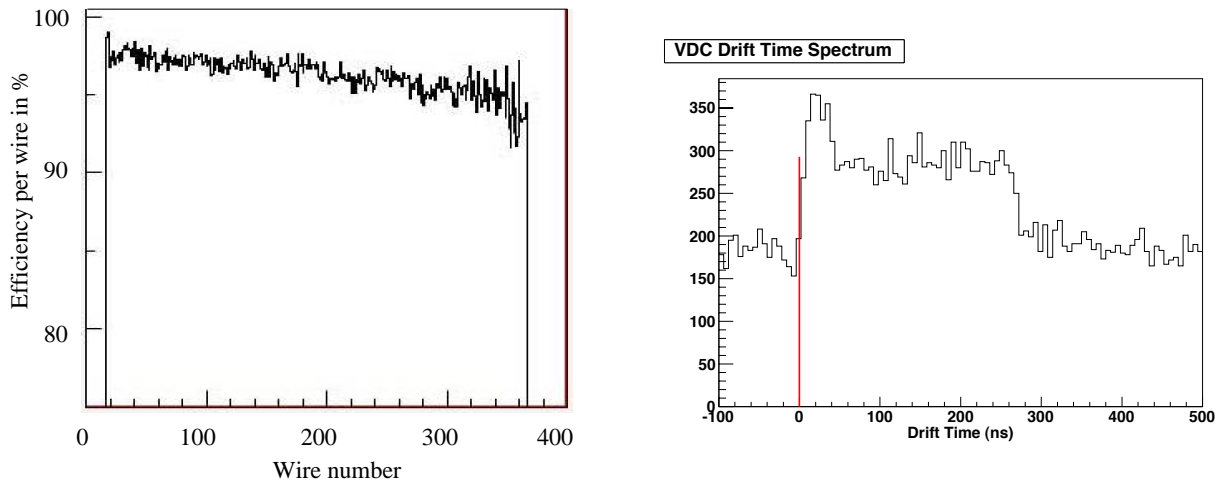


Figure 32: The VDC wire efficiency for high rate operation.

Figure 33: The VDC drift time for high rate operation.

it requires using appropriate front-end electronics. Such electronics were developed in our experiment [75] for the BigBite spectrometer. As proposed in PR12-10-0009, during the test run we installed these A/D cards and performed detailed tests of the VDC operation. The results of the test were presented by S. Riordan at the “Searching for a New Gauge Boson at JLab” workshop [72] and are summarized below.

- At the rate of 75 kHz/wire, which corresponds to a required track rate of 5 MHz in the electron arm, the VDC operated at reduced HV (3.5 kV) and wire current of 5 nA per cm of wire, which allows long term operation with a standard gas mixture used for VDC. The obtained efficiency is shown in Fig. 32.
- Drift time distribution for high rate data shows a normal profile, see Fig. 33.
- The off-line analysis showed that calibration drift time to coordinate is the same for low and high rate data, see Fig. 34.

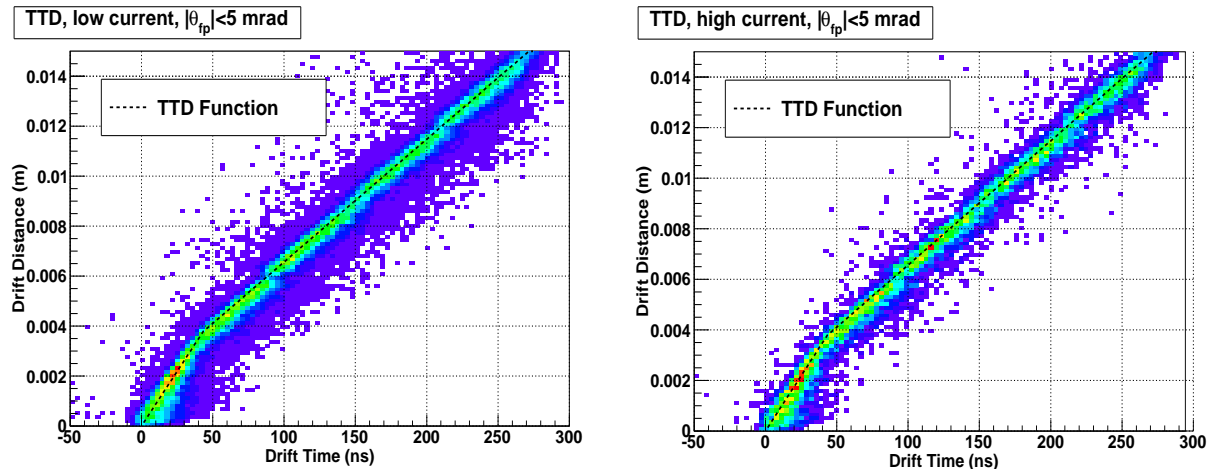


Figure 34: The VDC drift time to coordinate calibrations for the low rate (left plot) and high rate (right plot) operations.

- The cluster size shows reduction in high rate data, which is expected because during the short test the HV was not corrected for voltage drop on the protection resistor chain.
- Demonstrated reconstruction efficiency is about 60% for high rate operation (possibly as high as 75% with further analysis of the data).

8.11 Septum magnet (reviewer's comment 7)

We refer the reader to Section 4.3 for a discussion of the septum magnet and how it addresses the reviewer's comment 7.

8.12 Summary

Here we summarize what was presented above and reply to each concern identified by the reviewer in PAC35.

1. A multi-foil extended target based on 2.5 mm wide tungsten ribbons was constructed for use during the test run. Due to time constraints, it was not installed during the test run. It has all the advantages of the target design suggested in the previous version of this proposal to PAC35, but is simpler in its implementation. The details were presented in the report at the A' -boson workshop [72] and are also discussed further in Section 4.
2. An accuracy of 1 mrad in determining the central scattering angle between the two spectrometers is sufficient and easily achievable.
3. The test run data provided proof that the gas Cherenkov is useful in the trigger to help clean pions. An online rejection factor of 30 is sufficient and achievable at projected counting rates of the positron arm.

4. The background rates observed in the test run are in agreement with expectations in the original proposal.
5. The short coincidence time trigger was demonstrated during the test run.
6. The test run data was analyzed and provided concrete proof that the VDC can operate at a rate sufficiently high for the proposed experiment.
7. The study of the septum magnet via extensive TOSCA and SNAKE calculations confirmed that required uniformity will be provided.

The test run was a very productive way to demonstrate that the APEX experimental plan is sound and it helped speed up preparation of the new components that included the construction of the specialized target and acquiring the electronics for the trigger. The analysis of the small amount of science data is ongoing. We are performing a blind analysis to look for the A' signal, and we hope to unblind the data in the coming few months.

9 Conclusion

We request 34 days (33 days of beam time) to measure the electron-positron pair mass spectrum to search for a new gauge bosons A' in the mass range $65 \text{ MeV} < m_{A'} < 525 \text{ MeV}$ that has a weak coupling to electrons. Parametrizing this coupling by the ratio α'/α that controls the A' production cross-section, this experiment would probe α'/α as small as $\sim 9 \times 10^{-8}$ at masses from 65 to 300 MeV, and $\alpha'/\alpha \sim (2 - 3) \times 10^{-7}$ at masses up to 525 MeV, making it sensitive to production rates 100–1000 times lower than the best current limits set by measurements of the anomalous muon magnetic moment and by direct searches at BaBar. The experiment uses the JLab electron beam in Hall A at energies of approximately 1.1, 2.2, 3.3, and 4.4 GeV incident on a long (50 cm) multi-foil tungsten target and both arms of the High Resolution Spectrometer at angles of 5.0° relative to the nominal beam direction for the central target position. The experiment can determine the mass of an A' -boson to an accuracy of $\sim 1\text{--}2 \text{ MeV}$.

Constraints on new vector bosons with mass near 50 MeV – 1 GeV are remarkably weak. However, such light force carriers are well motivated theoretically, and several recent anomalies from terrestrial and satellite experiments suggest that dark matter has interactions with a new vector boson in precisely this mass range. The proposed experiment can probe this hypothetical particle with a sensitivity that is unrivaled by any existing experiment.

A Effective Photon Flux, Target Nucleus and Beam-Energy Dependence

In this appendix we summarize the formulas used in Section 3 for the reduced effective photon flux $\tilde{\chi}$, and highlight its dependence on the A' mass, target nucleus, and beam energy. The effective photon flux χ is obtained as in [51, 52] by integrating electromagnetic form-factors over allowed photon virtualities:

For a general electric form factor $G_2(t)$,

$$\chi \equiv \int_{t_{min}}^{t_{max}} dt \frac{t - t_{min}}{t^2} G_2(t) \quad (29)$$

(the other form factor, $G_1(t)$, contributes only a negligible amount in all cases of interest). Since we are dominated by a coherent scattering with $G_2 \propto Z^2$, it is useful to define a reduced photon flux,

$$\tilde{\chi} \equiv \chi/Z^2. \quad (30)$$

The integral in (29) receives equal contributions at all t , and so is logarithmically sensitive to $t_{min} = (m_{A'}/2E_0)^2$ and $t_{max} = m_{A'}^2$.

For most energies in question, $G_2(t)$ is dominated by an elastic component

$$G_{2,el}(t) = \left(\frac{a^2 t}{1 + a^2 t} \right)^2 \left(\frac{1}{1 + t/d} \right)^2 Z^2, \quad (31)$$

where the first term parametrizes electron screening (the elastic atomic form factor) with $a = 111 Z^{-1/3}/m_e$, and the second finite nuclear size (the elastic nuclear form factor) with $d = 0.164 \text{ GeV}^2 A^{-2/3}$. We have multiplied together the simple parametrizations used for each in [51]. The logarithm from integrating (29) is large for $t_{min} < d$, which is true for most of the range of interest. However, for heavy A' , the elastic contribution is suppressed and is comparable to an inelastic term,

$$G_{2,in}(t) = \left(\frac{a'^2 t}{1 + a'^2 t} \right)^2 \left(\frac{1 + \frac{t}{4m_p^2}(\mu_p^2 - 1)}{(1 + \frac{t}{0.71 \text{ GeV}^2})^4} \right)^2 Z, \quad (32)$$

where the first term parametrizes the inelastic atomic form factor and the second the inelastic nuclear form factor, and where $a' = 773 Z^{-2/3}/m_e$, m_p is the proton mass, and $\mu_p = 2.79$ [51]. This expression is valid when $t/4m_p^2$ is small, which is the case for $m_{A'}$ in the range of interest in this paper. At large t the form factors will deviate from these simple parameterizations but can be measured from data. One can show that the contribution from the other inelastic nuclear form factor $G_1(t)$ is negligible.

The resulting reduced form factor $\tilde{\chi}(m^2, E_0) = \chi/Z^2$ are plotted in the left panel of Figure 35 as a function of e^+e^- mass for various electron energies (1, 2, 3, and 4 GeV) incident on a Tungsten target. The relative efficiency of A' production in targets of different compositions but the same thickness in radiation lengths is given by the ratio

$$R(Z_1, Z_2) = \frac{X_0(Z_1)\chi(Z_1, t)/A(Z_1)}{X_0(Z_2)\chi(Z_2, t)/A(Z_2)}. \quad (33)$$

For example the ratio $R(Si, W)$ is shown in the right panel of Figure 35, again as a function of e^+e^- mass for beam energies between 1 and 4 GeV.

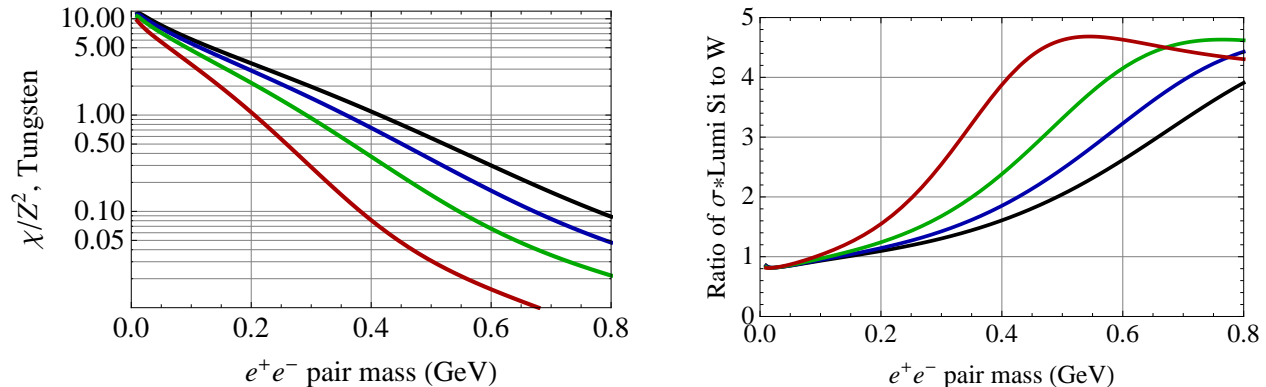


Figure 35: *Left:* The factor $\tilde{\chi} = \chi/Z^2$ defined in (30) and (29) as a function of e^+e^- mass for (bottom to top) 1, 2, 3, and 4 GeV incident electrons on a Tungsten target. *Right:* The ratio of (33) A' production rates per radiation length for Silicon and Tungsten targets, as a function of invariant mass and for beam energies (top to bottom at 0.4 GeV) 1, 2, 3, and 4 GeV incident electrons.

B Mass resolution

In this appendix, we briefly describe an estimate of the mass resolution of the spectrometer, which we used to calculate the sensitivity of the proposed experiment. Since we are looking for a small bump on the invariant mass spectrum distribution, an excellent mass resolution is essential to obtain a good reach in ϵ .

The mass resolution of the spectrometer, δ_m , is roughly given by

$$\left(\frac{\delta_m}{m}\right)^2 = \left(\frac{\delta_p}{p}\right)^2 + 0.5 \times \left(\frac{\delta_\theta}{\theta}\right)^2, \quad (34)$$

where δ_θ is the angular resolution of the electron or positron, and δ_p/p is the momentum resolution of the HRS, which is always less than 3×10^{-4} (in our estimates for the reach of ϵ , we take $\delta p/p$ to be equal to this upper bound). We have

$$(\delta_\theta)^2 = (\delta_{HRS})^2 + (\delta_\theta^{ms})^2, \quad (35)$$

where δ_{HRS} is the HRS angular resolution, which is ~ 0.5 mrad in the horizontal direction and ~ 1 mrad in the vertical direction. Moreover, δ_θ^{ms} represents the degradation of the resolution due to multiple Coulomb scattering in the target. It is given by the standard formula [54]

$$\delta_\theta^{ms} = \frac{13.6}{p[\text{MeV}]} \sqrt{\frac{t}{X_0}} \left[1 + 0.038 \ln \left(\frac{t}{X_0} \right) \right], \quad (36)$$

where t is the thickness in radiation lengths of the material along the path of the particle, X_0 is the radiation length of the target in g/cm^2 , and p is the momentum of particle in MeV.

For the proposed experiment, the thickness of the target along the direction of the beam line varies from $t = 0.007X_0$ to $t = 0.08X_0$. However, in the multi-foil target each electron-positron pair passes through only a single narrow foil with thickness 0.002–0.008 X_0 .

We note that for small α' , the lifetime of the A' is long enough to decay outside the target foils. There is thus no contribution from multiple-scattering in this case, leading to a better

mass resolution. We have not taken this into account in the sensitivity plots shown in this proposal, so the sensitivity of the experiment is slightly better than shown (although this is a small effect).

References

- [1] B. Holdom, *Two $U(1)$'s and Epsilon Charge Shifts*, *Phys. Lett.* **B166** (1986) 196.
- [2] <http://hallaweb.jlab.org/parity/prex/>.
- [3] M. Pospelov, *Secluded $U(1)$ below the weak scale*, 0811.1030.
- [4] **BABAR** Collaboration, B. Aubert *et al.*, *Search for Dimuon Decays of a Light Scalar in Radiative Transitions $Y(3S) \rightarrow \gamma A0$* , 0902.2176.
- [5] J. D. Bjorken *et al.*, *Search for Neutral Metastable Penetrating Particles Produced in the SLAC Beam Dump*, *Phys. Rev.* **D38** (1988) 3375.
- [6] E. M. Riordan *et al.*, *A Search for Short Lived Axions in an Electron Beam Dump Experiment*, *Phys. Rev. Lett.* **59** (1987) 755.
- [7] A. Bross *et al.*, *A Search for Shortlived Particles Produced in an Electron Beam Dump*, *Phys. Rev. Lett.* **67** (1991) 2942–2945.
- [8] J. D. Bjorken, R. Essig, P. Schuster, and N. Toro, *New Fixed-Target Experiments to Search for Dark Gauge Forces*, *Phys. Rev.* **D80** (2009) 075018, [0906.0580].
- [9] K. R. Dienes, C. F. Kolda, and J. March-Russell, *Kinetic mixing and the supersymmetric gauge hierarchy*, *Nucl. Phys.* **B492** (1997) 104–118, [hep-ph/9610479].
- [10] S. A. Abel and B. W. Schofield, *Brane-antibrane kinetic mixing, millicharged particles and SUSY breaking*, *Nucl. Phys.* **B685** (2004) 150–170, [hep-th/0311051].
- [11] M. J. Strassler and K. M. Zurek, *Echoes of a hidden valley at hadron colliders*, *Phys. Lett.* **B651** (2007) 374–379, [hep-ph/0604261].
- [12] S. A. Abel, M. D. Goodsell, J. Jaeckel, V. V. Khoze, and A. Ringwald, *Kinetic Mixing of the Photon with Hidden $U(1)$ s in String Phenomenology*, *JHEP* **07** (2008) 124, [0803.1449].
- [13] A. Ringwald, *From Axions to Other WISPs*, 0810.3106.
- [14] M. Baumgart, C. Cheung, J. T. Ruderman, L.-T. Wang, and I. Yavin, *Non-Abelian Dark Sectors and Their Collider Signatures*, *JHEP* **04** (2009) 014, [0901.0283].
- [15] N. Arkani-Hamed and N. Weiner, *LHC Signals for a SuperUnified Theory of Dark Matter*, *JHEP* **12** (2008) 104, [0810.0714].
- [16] C. Cheung, J. T. Ruderman, L.-T. Wang, and I. Yavin, *Kinetic Mixing as the Origin of Light Dark Scales*, 0902.3246.

- [17] D. E. Morrissey, D. Poland, and K. M. Zurek, *Abelian Hidden Sectors at a GeV*, 0904.2567.
- [18] A. Katz and R. Sundrum, *Breaking the Dark Force*, 0902.3271.
- [19] R. Essig, P. Schuster, and N. Toro, *Probing Dark Forces and Light Hidden Sectors at Low-Energy $e+e-$ Colliders*, 0903.3941.
- [20] **PAMELA** Collaboration, O. Adriani *et al.*, *Observation of an anomalous positron abundance in the cosmic radiation*, 0810.4995.
- [21] **The Fermi LAT** Collaboration, A. A. Abdo *et al.*, *Measurement of the Cosmic Ray $e+$ plus $e-$ spectrum from 20 GeV to 1 TeV with the Fermi Large Area Telescope*, 0905.0025.
- [22] J. Chang *et al.*, *An excess of cosmic ray electrons at energies of 300.800 GeV*, *Nature* **456** (2008) 362–365.
- [23] **H.E.S.S.** Collaboration, F. Aharonian *et al.*, *The energy spectrum of cosmic-ray electrons at TeV energies*, *Phys. Rev. Lett.* **101** (2008) 261104, [0811.3894].
- [24] **H.E.S.S.** Collaboration, F. Aharonian, *Probing the ATIC peak in the cosmic-ray electron spectrum with H.E.S.S.*, 0905.0105.
- [25] N. Arkani-Hamed, D. P. Finkbeiner, T. R. Slatyer, and N. Weiner, *A Theory of Dark Matter*, *Phys. Rev.* **D79** (2009) 015014, [0810.0713].
- [26] M. Pospelov and A. Ritz, *Astrophysical Signatures of Secluded Dark Matter*, *Phys. Lett.* **B671** (2009) 391–397, [0810.1502].
- [27] J. Hisano, S. Matsumoto, and M. M. Nojiri, *Explosive dark matter annihilation*, *Phys. Rev. Lett.* **92** (2004) 031303, [hep-ph/0307216].
- [28] J. March-Russell, S. M. West, D. Cumberbatch, and D. Hooper, *Heavy Dark Matter Through the Higgs Portal*, *JHEP* **07** (2008) 058, [0801.3440].
- [29] M. Cirelli, M. Kadastik, M. Raidal, and A. Strumia, *Model-independent implications of the $e+$, $e-$, anti-proton cosmic ray spectra on properties of Dark Matter*, *Nucl. Phys.* **B813** (2009) 1–21, [0809.2409].
- [30] I. Cholis, G. Dobler, D. P. Finkbeiner, L. Goodenough, and N. Weiner, *The Case for a 700+ GeV WIMP: Cosmic Ray Spectra from ATIC and PAMELA*, 0811.3641.
- [31] I. Cholis, D. P. Finkbeiner, L. Goodenough, and N. Weiner, *The PAMELA Positron Excess from Annihilations into a Light Boson*, 0810.5344.
- [32] Y. Cui, D. E. Morrissey, D. Poland, and L. Randall, *Candidates for Inelastic Dark Matter*, *JHEP* **05** (2009) 076, [0901.0557].
- [33] A. Sommerfeld *Ann. Phys.* **11** (1931) 257.
- [34] D. P. Finkbeiner, L. Goodenough, T. R. Slatyer, M. Vogelsberger, and N. Weiner, *Consistent Scenarios for Cosmic-Ray Excesses from Sommerfeld-Enhanced Dark Matter Annihilation*, 1011.3082.

- [35] O. Adriani *et al.*, *A new measurement of the antiproton-to-proton flux ratio up to 100 gev in the cosmic radiation*, 0810.4994.
- [36] D. Alves, S. R. Behbahani, P. Schuster, and J. G. Wacker, *Composite Inelastic Dark Matter*, 0903.3945.
- [37] D. Tucker-Smith and N. Weiner, *Inelastic dark matter*, *Phys. Rev.* **D64** (2001) 043502, [hep-ph/0101138].
- [38] S. Chang, G. D. Kribs, D. Tucker-Smith, and N. Weiner, *Inelastic Dark Matter in Light of DAMA/LIBRA*, 0807.2250.
- [39] R. Bernabei *et al.*, *Dark matter particles in the galactic halo: Results and implications from DAMA/NaI*, *Int. J. Mod. Phys.* **D13** (2004) 2127–2160, [astro-ph/0501412].
- [40] **DAMA** Collaboration, R. Bernabei *et al.*, *First results from DAMA/LIBRA and the combined results with DAMA/NaI*, *Eur. Phys. J.* **C56** (2008) 333–355, [0804.2741].
- [41] A. W. Strong *et al.*, *Gamma-ray continuum emission from the inner Galactic region as observed with INTEGRAL/SPI*, *Astron. Astrophys.* **444** (2005) 495, [astro-ph/0509290].
- [42] D. P. Finkbeiner and N. Weiner, *Exciting Dark Matter and the INTEGRAL/SPI 511 keV signal*, *Phys. Rev.* **D76** (2007) 083519, [astro-ph/0702587].
- [43] **CoGeNT** Collaboration, C. E. Aalseth *et al.*, *Results from a Search for Light-Mass Dark Matter with a P-type Point Contact Germanium Detector*, 1002.4703.
- [44] A. L. Fitzpatrick, D. Hooper, and K. M. Zurek, *Implications of CoGeNT and DAMA for Light WIMP Dark Matter*, *Phys. Rev.* **D81** (2010) 115005, [1003.0014].
- [45] R. Essig, J. Kaplan, P. Schuster, and N. Toro, *On the Origin of Light Dark Matter Species*, 1004.0691.
- [46] **Muon G-2** Collaboration, G. W. Bennett *et al.*, *Final report of the muon E821 anomalous magnetic moment measurement at BNL*, *Phys. Rev.* **D73** (2006) 072003, [hep-ex/0602035].
- [47] **The BABAR** Collaboration, B. Aubert, *Search for Dimuon Decays of a Light Scalar in Radiative Transitions $Y(3S) \rightarrow \gamma A0$* , 0902.2176.
- [48] M. Reece and L.-T. Wang, *Searching for the light dark gauge boson in GeV-scale experiments*, 0904.1743.
- [49] **KTeV** Collaboration, E. Abouzaid *et al.*, *Measurement of the rare decay $\pi^0 \rightarrow e^+ e^-$* , *Phys. Rev.* **D75** (2007) 012004, [hep-ex/0610072].
- [50] Bossi, F., private communication.
- [51] K. J. Kim and Y.-S. Tsai, *Improved Weizsäcker-Williams method and its application to lepton and W-boson pair productions*, *Phys. Rev.* **D8** (1973) 3109.

- [52] Y.-S. Tsai, *Pair Production and Bremsstrahlung of Charged Leptons*, *Rev. Mod. Phys.* **46** (1974) 815.
- [53] Y.-S. Tsai, *Axion Bremsstrahlung by and electron beam*, *Phys. Rev.* **D34** (1986) 1326.
- [54] **Particle Data Group** Collaboration, C. Amsler *et al.*, *Review of particle physics*, *Phys. Lett.* **B667** (2008) 1.
- [55] *NIM A522* **A522** (2004) 294–346.
- [56] G2P (<http://hallaweb.jlab.org/experiment/E08-027/>) E08-027: Measurement of g2p and the Longitudinal-Transverse Spin Polarizability A. Camsonne, J.P. Chen, D. Crabb, K. Slifer (spokespeople).
- [57] P. Brindza, “Septum & Radiation” at “Searching for a New Gauge Boson at JLab” (Sept 2010)
http://conferences.jlab.org/boson2010/Tuesday/Brindza%20APEX_PB.pptx .
- [58] J. Huang, “HRS Parameters and Optics” at “Searching for a New Gauge Boson at JLab” (Sept 2010),
<http://conferences.jlab.org/boson2010/Tuesday/Apex%20Optics.Huang.pptx> .
- [59] E. Jensen, “HRS Trigger and PID” at “Searching for a New Gauge Boson at JLab” (Sept 2010),
<http://conferences.jlab.org/boson2010/Tuesday/HRS%20Fast%20Trigger%20and%20PID%20Capabi>
- [60] S. Riordan, “HRS wire chamber tracking” at “Searching for a New Gauge Boson at JLab” Workshop (Sept 2010),
http://conferences.jlab.org/boson2010/Tuesday/riordan_apexvdc.pdf.
- [61] I. Rachek *et al.* *Hall A annual report* (2007) 13–15.
- [62] J. Alwall *et al.*, *MadGraph/MadEvent v4: The New Web Generation*, *JHEP* **09** (2007) 028, [0706.2334].
- [63] D. Wiser *Ph.D. thesis*, *University of Wisconsin* (1977).
- [64] V. Budnev *et al.* *Phys. Rep.* **15C** (1975) 181.
- [65] J. O’Connell and J. Lightbody, *Computer codes QFS and EPC*, *Comp. in Phys.* **May-June 57** (1998).
- [66] E04-012 (<http://hallaweb.jlab.org/experiment/E04-012/>), Y. Qiang, private communication.
- [67] H. Burfeindt *et al.* *Physics Letters* **43B** (1973) 345.
- [68] H. Burfeindt *et al.* *Nucl. Phys.* **B74** (1974) 189.
- [69] A. Boyarsli *et al.* *PRD* **14** (1976) 1733.
- [70] P. Degtyarenko, M. Kossov, and H.-P. Wellisch, *Chiral Invariant Phase Space Event Generator, I. Nucleon-antinucleon annihilation at rest*, *Eur. Phys. J. A* **8** (2000) 217.

- [71] Y. S. Tsai and V. Whitis, *Thick-target bremsstrahlung and target considerations for secondary-particle production by electrons*, *Phys. Rev.* **149** (Sep, 1966) 1248–1257.
- [72] W. on “Searching for a New Gauge Boson at JLab” (Sept 2010) <http://conferences.jlab.org/boson2010/program.html>.
- [73] Y. Qiang, P. 166 in PhD thesis, MIT.
- [74] **Particle Data Group** Collaboration, K. Nakamura *et al.*, *Review of particle physics*, *J. Phys.* **G37** (2010) 075021.
- [75] <http://hallaweb.jlab.org/experiment/E02-013/> E02-013: Neutron form factor at high momentum transfer. G. Cates, N. Liyanage, B. Wojtsekhowski (spokespeople).